

C9orf72 BAC Mouse Model with Motor Deficits and Neurodegenerative Features of ALS/FTD

Highlights

- C9orf72 BAC mice with behavioral, neurodegenerative, and molecular features of ALS/FTD
- These mice express C9orf72 sense and upregulated antisense transcripts
- Antisense RNA foci accumulate preferentially in ALS/FTD-vulnerable cell populations
- RAN aggregates increase with age and disease with TDP-43 aggregates at end stage

Authors

Yuanjing Liu, Amrutha Pattamatta, Tao Zu, ..., David R. Borchelt, Anthony T. Yachnis, Laura P.W. Ranum

Correspondence

ranum@ufl.edu

In Brief

Liu et al. report the generation of the first C9orf72 BAC mouse model that recapitulates the molecular, behavioral, and neurodegenerative features of ALS/FTD. Antisense RNA foci accumulate in vulnerable regions, and RAN protein accumulation increases with age and disease.



C9orf72 BAC Mouse Model with Motor Deficits and Neurodegenerative Features of ALS/FTD

Yuanjing Liu,^{1,2} Amrutha Pattamatta,^{1,2} Tao Zu,^{1,2} Tammy Reid,^{1,2} Olgert Bardhi,^{1,2} David R. Borchelt,^{1,3,6} Anthony T. Yachnis,⁴ and Laura P.W. Ranum^{1,2,5,7,*}

¹Center for NeuroGenetics

²Department of Molecular Genetics and Microbiology

³Department of Neuroscience

⁴Department of Pathology, Immunology, and Laboratory Medicine

⁵Department of Neurology

⁶Center for Translational Research in Neurodegenerative Diseases, College of Medicine

⁷Genetics Institute

University of Florida, Gainesville, FL 32610, USA

*Correspondence: ranum@ufl.edu

<http://dx.doi.org/10.1016/j.neuron.2016.04.005>

SUMMARY

To define how the *C9orf72* GGGGCC expansion mutation causes ALS/FTD and to facilitate therapy development, a mouse model that recapitulates the molecular and phenotypic features of the disease is urgently needed. Two groups recently reported BAC mouse models that produce RNA foci and RAN proteins but, surprisingly, do not develop the neurodegenerative or behavioral features of ALS/FTD. We now report a BAC mouse model of *C9orf72* ALS/FTD that shows decreased survival, paralysis, muscle denervation, motor neuron loss, anxiety-like behavior, and cortical and hippocampal neurodegeneration. These mice express *C9orf72* sense transcripts and upregulated antisense transcripts. In contrast to sense RNA foci, antisense foci preferentially accumulate in ALS/FTD-vulnerable cell populations. RAN protein accumulation increases with age and disease, and TDP-43 inclusions are found in degenerating brain regions in end-stage animals. The ALS/FTD phenotypes in our mice provide a unique tool that will facilitate developing therapies targeting pathways that prevent neurodegeneration and increase survival.

INTRODUCTION

Amyotrophic lateral sclerosis (ALS) is a debilitating neurodegenerative disease that causes degeneration of upper and lower motor neurons, which leads to paralysis, respiratory failure, and death (Rowland and Schneider, 2001). Frontotemporal dementia (FTD) is a type of early onset dementia caused by degeneration of the frontal and anterior temporal lobes causing cognitive deficits and behavioral and language abnormalities (McKhann et al., 2001). Symptoms include loss of empathy, stereotypic behavior, apathy, and/or disinhibition. A hexanucleotide (GGGGCC,

G4C2) repeat expansion in an intron of *C9orf72* is the most frequent reported genetic cause of ALS and FTD (DeJesus-Hernandez et al., 2011; Renton et al., 2011). This discovery was exciting because it genetically linked ALS and FTD to each other and to a larger group of microsatellite expansion diseases (Cleary and Ranum, 2014). Building on research from other microsatellite diseases (Cleary and Ranum, 2013; Goodwin and Swanson, 2014; Orr and Zoghbi, 2007; Ranum and Cooper, 2006), several possible disease mechanisms have emerged for *C9orf72* ALS/FTD, including (1) loss of function of the *C9orf72* protein caused by haploinsufficiency of *C9orf72* mRNA in patients with expansions (DeJesus-Hernandez et al., 2011); (2) RNA gain of function in which sense or antisense expansion RNAs (DeJesus-Hernandez et al., 2011; Zu et al., 2013) sequester one or more RNA binding proteins, compromising their physiological function (Freibaum et al., 2015; Goodwin and Swanson, 2014; Jovičić et al., 2015; Zhang et al., 2015); and (3) repeat-associated non-ATG (RAN) translation (Zu et al., 2011) of the expansion RNAs, which gives rise to six RAN proteins (poly-GlyAla [GA], poly-GlyArg [GR], and poly-GlyPro [GP] in the sense direction, and poly-GlyPro [GP], poly-ProArg [PR], and poly-ProAla [PA] in the antisense direction) that accumulate in human C9(+) autopsy tissue (Ash et al., 2013; Mori et al., 2013; Zu et al., 2013).

A number of models have been generated to understand the molecular events that lead to *C9orf72* ALS/FTD (Ciura et al., 2013; Freibaum et al., 2015; Jovičić et al., 2015; Kwon et al., 2014; Lagier-Tourenne et al., 2013; Mizielinska et al., 2014; Suzuki et al., 2013; Therrien et al., 2013; Zhang et al., 2015). Knockout of the *C9orf72* ortholog (*3110043O21Rik*) at embryonic day (E)10.5 in neurons and glia failed to cause neurodegenerative changes, arguing that *C9orf72* loss of function is not sufficient to cause disease (Koppers et al., 2015). Further support for a gain-of-function mechanism is provided by adeno-associated virus (AAV)-mediated overexpression of a minigene containing 66 G4C2 repeats in mice that leads to mild neurodegeneration in the cortex and cerebellum, but not the severe phenotypes and paralysis found in ALS/FTD (Chew et al., 2015). While there is growing evidence that overexpression of *C9orf72* RNAs or RAN proteins can cause gain-of-function

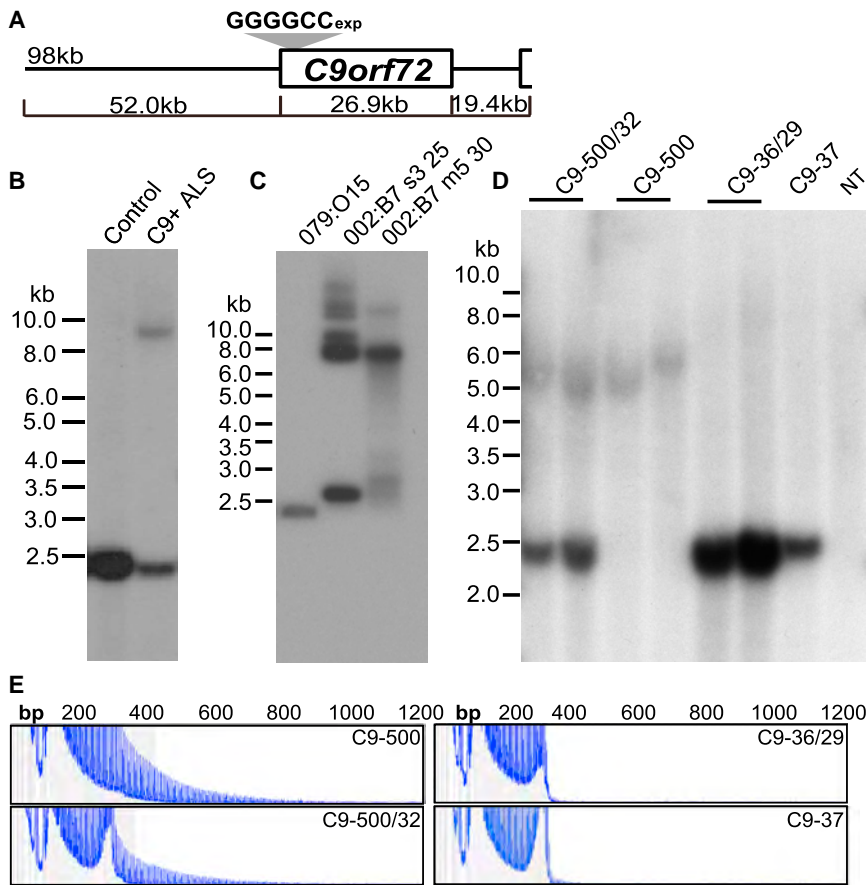


Figure 1. Generation of *C9orf72* BAC Transgenic Lines with G4C2 Expansion Mutations

(A) Schematic of the BAC construct showing the relative position of the *C9orf72* gene and flanking sequence.

(B) Southern blot of genomic DNA from patient lymphoblastoid cell line (LCL) (~1,200 repeats) used to generate the BAC library and a control LCL.

(C) Southern blot of *C9orf72*-positive BACs with the normal allele (079:015) or expansion containing subclones (002:B7 s3 25 and 002:B7 m5 30) of the expansion BAC used for pronuclear injections.

(D) Southern blot showing the repeat size in mice from four different BAC transgenic mouse lines: two F1 littermates from each of the C9-500/32, C9-500, and C9-36/29 founders and one F1 mouse from the C9-37 line.

(E) Fluorescently labeled repeat-primed PCR products confirming that two of the lines (C9-500 and C9-500/32) contain large G4C2 expansions while the other two lines (C9-36/29 and C9-37) contain shorter expansions.

effects (Chew et al., 2015; Kwon et al., 2014; Mizielinska et al., 2014; Wen et al., 2014), there is an urgent need for a transgenic mouse that develops the clinical and neurodegenerative features of ALS/FTD by driving sense and antisense gene expression at levels and in spatial/temporal expression patterns found in patients. Recently, two groups reported the development of *C9orf72* bacterial artificial chromosome (BAC) transgenic mouse models that accumulate RAN proteins and RNA foci but do not develop the clinical features of ALS/FTD (O'Rourke et al., 2015; Peters et al., 2015).

Here, we describe a novel BAC transgenic mouse model containing the full-length *C9orf72* gene and substantial flanking sequence to drive expression of sense and antisense transcripts using the endogenous human promoters. In contrast to other *C9orf72* mouse models (Chew et al., 2015; O'Rourke et al., 2015; Peters et al., 2015; Suzuki et al., 2013), our mice show decreased survival as well as phenotypic, neuropathological, and molecular hallmarks of *C9orf72* ALS/FTD.

RESULTS

Generation of *C9orf72* BAC G4C2 Expansion Mice

To understand the molecular mechanisms and disease course of *C9orf72* ALS/FTD, we developed a BAC transgenic mouse model. The BAC construct shown in Figure 1A was selected for pronuclear injection because it contains the full-length human

C9orf72 gene and no other annotated genes. PCR amplification and sequencing using the pCC1-F and pCC1-R primers (Table S1, available online) were performed to identify the 5' and 3' ends of the BAC insertion, which showed the 002:B7 BAC contains a 98 kb insert from chromosome 9: 27,527,137 bp to 27,625,470 bp (Human Genome,

February 2009, GRCh37/hg19). This BAC contains 2 kb of the nearby *Mps one binder kinase activator 3B (MOB3B)* gene, but not the ATG initiation site for the *MOB3B* open reading frame (ORF), nor any portion of the neighboring *interferon kappa, IFNK* gene.

The substantial flanking sequence (52 kb 5' and 19 kb 3') of *C9orf72* is likely to contain the regulatory regions needed to control expression of the sense and antisense transcripts in temporal and spatial patterns that mimic expression in the human disease. This construct was isolated from a patient-derived BAC library (Figure S1A) developed from a lymphoblastoid cell line (LCL) containing an expansion mutation of ~1,200 repeats (Figure 1B). Because the repeat expansion in the original 002:B7 bacterial clone was highly unstable (Figure S1B), we prepared 30 subcultures under different conditions and selected two subclones that retained the expansion. BAC DNA extracted from these subclones was used for pronuclear injections (Figures 1C and S1C). In general, smaller colonies grown at lower temperatures more efficiently retained the expansion mutation. Additionally, in both conditions, the majority of subclones showed a bimodal distribution with repeat sizes of ~40 and ~500. Eleven founder mice were identified; two of these contained expansions of ~500 repeats and nine had shorter expansions (30–40 repeats). The number of transgene copies in these lines was estimated by southern blot using a probe outside the repeat region (data not shown). Four *C9orf72* BAC lines (C9-BAC) were

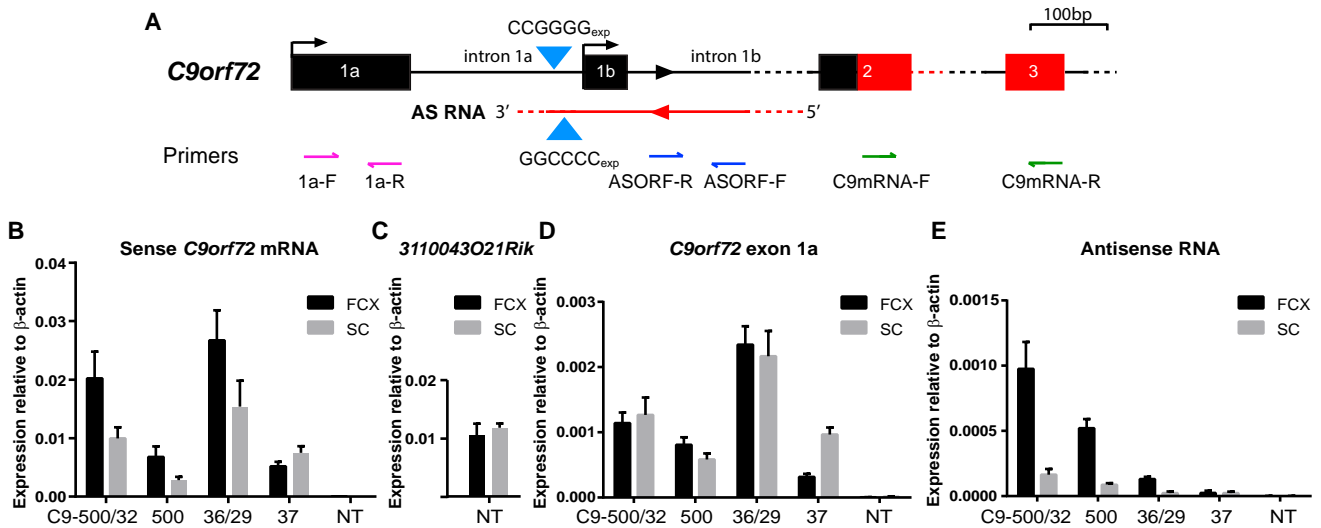


Figure 2. Sense and Antisense Expression of the *C9orf72* BAC Transgene in Frontal Cortex and Spinal Cord

(A) Schematic diagram showing primers used to detect *C9orf72* sense and antisense transcripts. Black boxes indicate noncoding regions and red boxes indicate coding regions. Primer sets that amplify specific transcript variants are indicated at their relative locations: exon 1a containing *C9orf72* sense (1a-F, R), antisense transcripts (ASORF-R, F), and all three *C9orf72* sense variants (C9mRNA-F, R). Figure drawn to scale.

(B) qRT-PCR of all three isoforms of human sense *C9orf72* from transgenic and nontransgenic (NT) mice, $n = 4$ mice per group.

(C) qRT-PCR of the mouse *C9orf72* ortholog (*3110043O21Rik*) in NT mice, $n = 4$.

(D) qRT-PCR of *C9orf72* exon 1a sense repeat-containing transcripts, $n = 4$ per line.

(E) qRT-PCR showing antisense transcripts are highly elevated in lines with long expansions (C9-500/32 and C9-500) and moderately elevated in C9-36/29 mice compared to the C9-37 line, $n = 4$ per line.

established for further analyses: C9-500/32 (two transgene copies, one with ~ 500 and the other with 32 repeats), C9-500 (one copy with ~ 500 repeats), C9-36/29 (four transgene copies with repeat sizes of 36 and 29 detected), and C9-37 (one copy with 37 repeats) (Figures 1D, 1E, and S2A). In the multiple copy lines (C9-500/32 and C9-36/29), the transgenes always segregated together, indicating they integrated at a single insertion site. Repeat length is relatively stable in somatic tissues (brain and tail) (Figure S2B), and the transgene can be transmitted from generation to generation. Some intergenerational instability of the longer repeat tracts was found, which was more evident in the C9-500/32 line (Figure S2C). To maintain these expansion lines, we screen breeders by southern blotting and select those that maintain the long repeat.

Sense and Antisense *C9orf72* Expression in C9-BAC Lines

Since frontal lobe and lumbar spinal cord are prominently affected in ALS/FTD, sense and antisense transgene expression in these regions was quantified by qRT-PCR using several primer sets (Figure 2A; Table S1). Data generated using primers flanking constitutive exons 2 and 3 show that the overall levels of *C9orf72* sense transcripts expressed from human BAC transgene correlate with copy number and that similar levels of the mouse *C9orf72* ortholog (*3110043O21Rik*) relative to β -actin are found (Figures 2B and 2C). qRT-PCR using primers in exon 1a, designed to selectively amplify repeat-containing *C9orf72* transcripts, shows that the G4C2 expansion is expressed in all four transgenic lines with the highest expression levels in the four-copy C9-36/29 line (Figure 2D). Additionally, we show antisense

transcripts in the frontal cortex are ~ 40 -fold higher in the C9-500/32 line and ~ 22 -fold higher in the C9-500 line compared to the C9-37 line. Antisense levels are also elevated in the four-copy C9-36/29 line with levels ~ 5 fold higher than the C9-37 line (Figure 2E). This upregulation recapitulates the increased expression of antisense transcripts (~ 10 - to 300-fold) seen in autopsy tissue from C9(+) versus control ALS patients (Zu et al., 2013). A similar trend of antisense upregulation (4- to 7-fold) is also seen in spinal cord in the C9-500/32 and C9-500 lines, compared to C9-37, but the overall levels are lower. These data indicate that the expansion mutation regulates antisense expression and that this upregulation is pronounced in the frontal cortex. Time course studies of *C9orf72* transcripts in the C9-500 line show no significant differences in levels of expression between post-natal day (P1–P3) and 5 months of age (Figure S3A). Similarly, no differences in expression were found between male and female expansion mice in any of the lines (Figures S3B and S3C).

In summary, we used endogenous human regulatory regions in a large insert BAC construct to drive expression of the *C9orf72* expansion mutation in our mice. We show sense transcripts are expressed in all four lines and, similar to C9(+) patients (Zu et al., 2013), antisense transcripts are highly upregulated in the two lines of mice with 500 repeats.

C9-BAC Mice Show G4C2 Repeat Length- and Expression-Dependent Disease Phenotypes Gait Abnormalities

From birth to ~ 16 weeks of age, animals from all four transgenic lines appear normal, with no overt cage behavior abnormalities

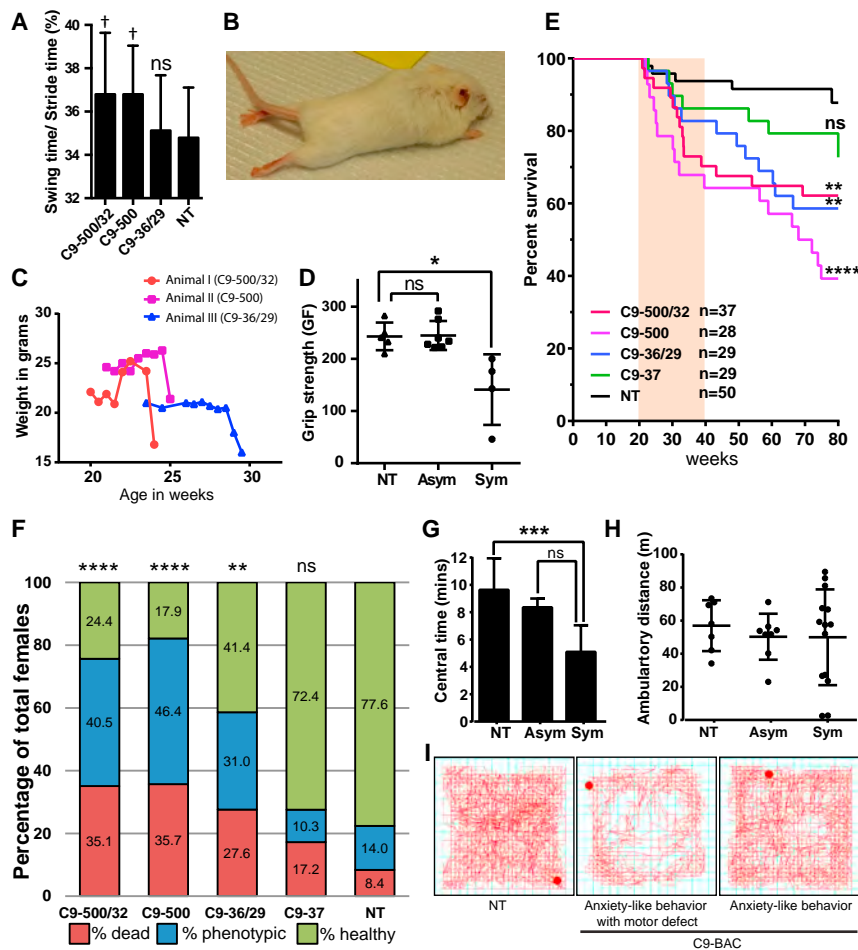


Figure 3. C9-BAC Mice Show Gait Abnormalities, Paralysis, Anxiety-like Behavior, and Decreased Survival

(A) Gait abnormalities in C9-BAC mice at 4 months of age. Representative example shows percentage of swing time/stride time of the hindlimbs is reduced in the C9-500/32 and C9-500 long repeat lines, but not the C9-36/29 line, compared to NT littermates. C9-500/32, $n = 16$; C9-500, $n = 14$; C9-36/29, $n = 11$; NT, $n = 21$; mean \pm SD, multiple t test, † significant, desired FDR (false discovery rate) set to 5%, ns = not significant.

(B) Representative image of an acute end-stage C9-500/32 mouse (7 months old) with hindlimb paralysis.

(C) Graph illustrating examples of rapid weight loss seen in acute end-stage C9-BAC animals (red, C9-500/32 mouse; pink, C9-500 mouse; and blue, C9-36/29 mouse).

(D) Grip strength in acute end-stage and asymptomatic (Asym) mice compared to NT littermates. NT, $n = 5$; Asym, $n = 7$; acute end-stage, $n = 4$; mean \pm SD, unpaired t test, * $p < 0.05$.

(E) Kaplan-Meier survival curve of female C9-BAC mice shows decreased survival of the C9-500, C9-500/32, and C9-36/29 lines, but not the C9-37 line, compared to NT littermates. Disease onset window observed in the majority of sick animals is indicated by the shaded region. Gehan-Breslow-Wilcoxon test, ** $p \leq 0.01$, **** $p \leq 0.0001$, ns $p \geq 0.05$.

(F) Population census plot indicates the percentage of female mice in each line that are dead (red), phenotypic (blue), or healthy (green) at 1 year of age compared to NT littermates, with differences found between C9-500/32, C9-500, and C9-36/29 lines compared to NT controls. C9-500/32, $n = 37$; C9-500, $n = 28$; C9-36/29, $n = 29$; C9-37, $n = 29$; NT, $n = 50$. Chi-square test, ** $p \leq 0.01$, **** $p \leq 0.0001$, ns $p \geq 0.05$.

(G) Open field test showing significantly shorter time spent in central region of the test chamber in aged symptomatic mice compared to NT littermates. No differences were seen in asymptomatic gene-positive animals compared to NT littermates. NT, $n = 7$; Asym, $n = 8$; Sym, $n = 14$; mean \pm SD, unpaired t test, *** $p \leq 0.001$, ns $p \geq 0.05$.

(H) Total ambulatory distance shows a subset of the symptomatic mice had both motor deficits and anxiety-like behavior, while the other animals showed exclusively anxiety-like phenotypes.

(I) Representative traces showing the path of the animals in the open field apparatus (snapshot taken at 15 min).

or differences in weight at weaning compared to nontransgenic (NT) littermates. At 16 weeks, DigiGait analyses show transgene-positive mice from the C9-500/32 and C9-500 lines develop hindlimb gait abnormalities. Out of 42 gait parameters, mice from the C9-500/32 and C9-500 lines showed 14 and 4 significant changes compared to NT littermates, respectively. Mice from the C9-36/29 line did not show significant changes in gait at ~16 weeks compared to NT animals (Table S2). Data from one of these gait abnormalities, increased percentage of swing time/stride time, are shown in Figure 3A.

Decreased Survival

Between 20 and 40 weeks of age, a subset of female mice (~30%–35%) from the C9-500/32 and C9-500 lines develop an acute, rapidly progressive disease characterized by inactivity, labored breathing, sudden weight loss (20%–25% in 2–3 days), hindlimb weakness, paralysis, and dramatic decreases in survival compared to NT littermates ($p < 0.01$ and $p < 0.0001$, respectively)

(Figures 3B–3E; Movies S1 and S2). Additionally, a subset of female mice from the high-expression four-copy C9-36/29 line show similar acute phenotypes, but with delayed onset of motor symptoms and the majority of deaths occurring later, after 40 weeks of age ($p \leq 0.01$ C9-36/29 versus NT). In contrast, female mice from the single-copy C9-37 line showed no significant differences in survival compared to NT controls (Figure 3E).

Progressive Phenotypes

In addition to the acute disease described above, a large percentage of the remaining animals develop a milder and slower progressive disease characterized by kyphosis, reduced activity, hyperactivity when provoked, clapping, and intermittent seizures (Movie S3). These phenotypes are progressive and can, but do not necessarily, cause premature death. To quantitate the percentage of mice with these disease symptoms, we evaluated the phenotypes of approximately 300 male and female mice from four C9-BAC lines and their NT littermates. At 1 year

of age, 35.1%, 35.7%, and 27.6% of female mice from the C9-500/32, C9-500, and C9-36/29 lines had died, and an additional 40.5%, 46.4%, and 31% had developed symptoms. No significant differences in survival were seen between animals in the C9-37 line and NT controls (Figure 3F). In contrast to female mice, males from the C9-500/32 and C9-500 expansion lines do not show decreased survival compared to NT males at 1 year (Figures S4A and S4B), but a large proportion of these animals (~43%–45%) developed phenotypes by 1 year of age ($p < 0.05$) (Figures S4C and S4D). These phenotypes were similar to those found in the slow progressive female mice. No significant differences in survival or phenotype were seen in males from the C9-36/29 or C9-37 lines compared to the NT controls (Figure S4).

Open Field Analysis

Open field analyses of the older symptomatic male and female mice (1–1.5 years) and age-matched littermates show symptomatic mice spend 50% less time in the central region of the chamber compared to their asymptomatic and NT littermates, a phenotypic indication of anxiety-like behavior (Figures 3G and 3I) (Keum et al., 2016; Miller et al., 2010; Milner and Crabbe, 2008). Additionally, a subset of these symptomatic animals showed marked decreases in ambulation (Figures 3H and 3I).

In summary, lines with long repeats (C9-500 and C9-500/32) show significant decreases in survival, and a large proportion of animals die or develop phenotypic abnormalities by 1 year of age (76%–82% of females and 50% of males). Additionally, decreased survival and disease phenotypes are also found in females from the high-expression four-copy C9-36/29 line, but the disease is generally later onset and less penetrant at 1 year of age compared to disease in females from the long expansion lines. In contrast, no significant phenotypic differences were found in male mice from the C9-36/29 line compared to NT males. These data indicate shorter expansions (36 and 29 repeats) at higher levels are sufficient to cause the disease in female mice. Comparisons between the C9-500 and C9-37 lines, which express *C9orf72* transcripts at comparable levels, show the development of disease is length dependent. Additionally, the development of similar disease phenotypes and penetrance in the C9-500 and C9-500/32 expansion lines indicates that these phenotypes are not caused by an insertion effect.

Our subsequent analyses focused on female mice (20–40 weeks) from the C9-500/32, C9-500, and C9-36/29 lines that developed the acute, rapidly progressing disease (referred to as “acute”) and aged (52–72 weeks) mice from the C9-500/32 and C9-500 lines that have slow disease progression (referred to as “slow progressive”).

C9-BAC Mice Develop Motor Neuron Disease

To determine if the C9-BAC mice develop motor neuron disease, we examined the neuromuscular junctions in our mice. Animals with acute disease, which had reached end stage between 20 and 40 weeks, showed marked denervation of the neuromuscular junctions in the tibialis anterior (66%) and diaphragm (49%) muscles compared to 4.5% and 3.9% in NT littermates ($p < 0.0001$ and $p = 0.02$, respectively) (Figure 4A). No changes were found between asymptomatic C9-500 and C9-500/32 mice and age-matched NT controls (Figure S5A). Despite the

dramatic loss of axon terminals, most neuromuscular junctions retained their normal “pretzel-shaped” morphology. Immunohistochemical (IHC) staining of muscle with myosin-32 antibody showed mild muscle abnormalities with focal sites of pathology. These changes include atrophic fibers, sharp angular fibers, and pyknotic nuclear clumps in fast-twitch muscle fibers, typical of denervation (Figure S5B). The relative preservation of the neuromuscular junction morphology and focal, but not widespread, skeletal muscle atrophy are consistent with the rapid disease progression in these mice, and suggest that neuronal loss precedes muscle pathology. In the slow progressive mice, more subtle neuromuscular junction abnormalities are seen. These include increased axonal swelling and axon terminal sprouting, indicative of degeneration and regeneration (Figure S5C).

To examine the motor axons projecting from the lumbar spinal cord, we quantified axonal size within the lumbar-4 (L4) ventral spinal roots. As shown in Figure 4B, acute end-stage animals have a loss of axonal integrity with increased numbers of small axons ($< 4 \mu\text{m}$ in diameter), indicative of degeneration and regeneration, and fewer large caliber α -axons ($\geq 4 \mu\text{m}$ in diameter). In the slower progressing animals, similar but milder phenotypes are also found in the spinal roots with an overall shift to smaller fiber sizes (Figure S5D).

Pathological evaluation of the ventral horn of the lumbar spinal cord in acute end-stage mice showed a significant loss in motor neurons stained by choline acetyltransferase (ChAT) (Figure 4C), with cresyl-violet (CV) staining of the lumbar spinal cord corroborating this finding (Figure S6A). Additionally, we observed atrophic and vacuolated motor neurons (Figure 4D). Lower motor neuron loss was also found in the slow progressing animals (Figure S6B). Additionally, we observed degeneration, pyknosis, and vacuolization of the large pyramidal neurons in layer V of the motor cortex in acute end-stage mice, a region of the brain containing upper motor neurons (Figure 4E).

In summary, these results show C9-BAC mice mimic ALS with degenerative changes seen throughout the motor unit. These changes include (1) degeneration of the large pyramidal neurons in layer V of the motor cortex, (2) degeneration of the lower motor neurons that send their corresponding axons into the ventral spinal roots, and (3) degeneration of the axons that terminate in target skeletal muscles at the neuromuscular junctions.

C9-BAC Mice Show Neurodegenerative Changes Characteristic of ALS/FTD

Because the *C9orf72* expansion mutation can cause both ALS and FTD, and pathology has been reported throughout the CNS, we examined our mice for additional signs of neuropathology. We found dramatic changes in acute end-stage animals ($n = 6$) that were not found in a large cohort ($n = 16$) of asymptomatic transgene-positive littermates (8–20 weeks). In acute end-stage mice, hematoxylin and eosin (H & E), and CV and NeuN staining show extensive neuronal loss, pyknosis, and abundant vacuolization in layers II/III throughout the cortex and in layer V of the motor cortex compared to NT mice (Figure 5A). Quantification of CV-stained neurons showed ~75% decrease in layer II/III neurons and ~57% decrease in layer V of the motor cortex (Figure 5B). In contrast, no overt differences

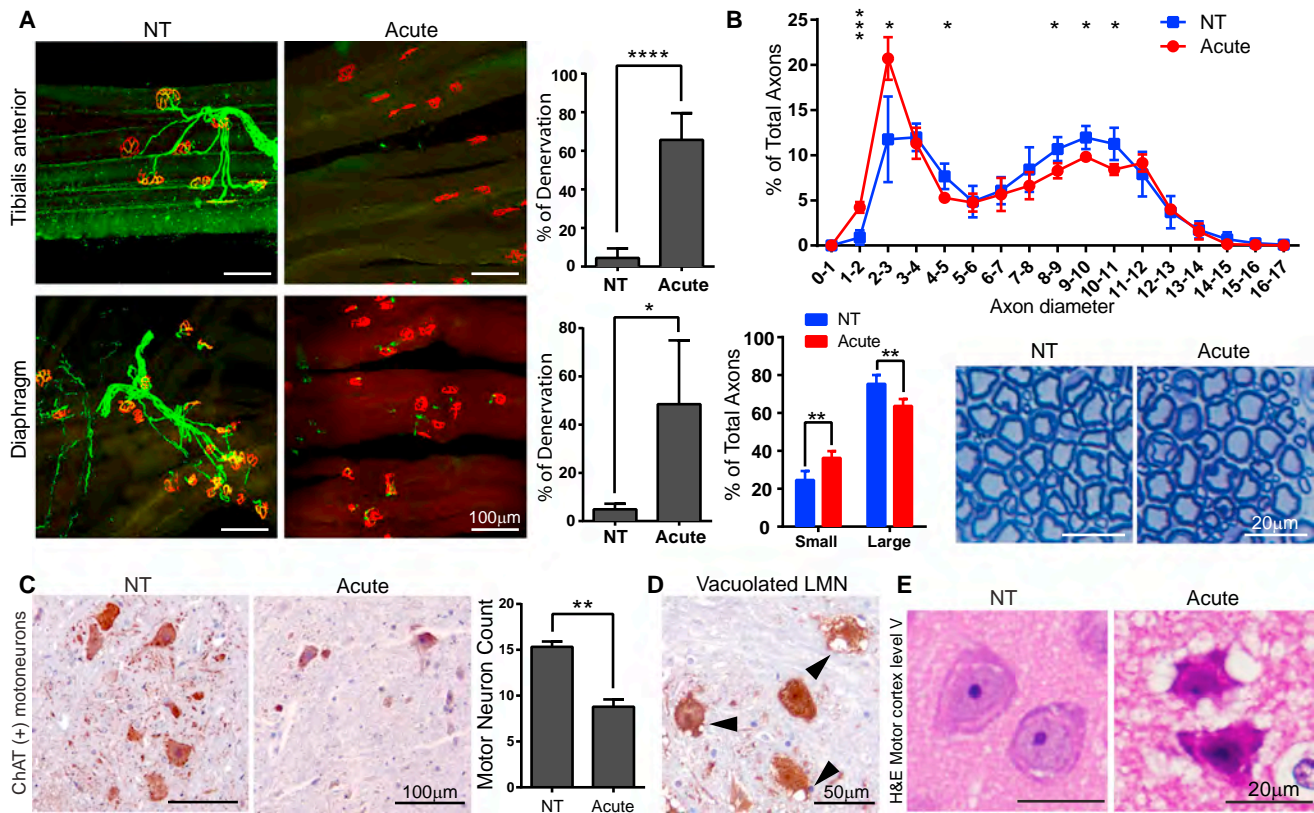


Figure 4. C9-BAC Mice Develop Motor Neuron Disease

(A) Denervation of tibialis anterior muscle and diaphragm in acute end-stage C9-BAC mice. Neuromuscular junctions (red), acetylcholine receptors labeled with α -bungarotoxin tetramethylrhodamine conjugate, and motor axons and synapses (green), labeled with anti-neurofilament H antibody. Quantifications were performed for ~100 neuromuscular junctions per animal. NT, $n = 3$; acute end-stage, $n = 3$; mean \pm SD, unpaired t test, $*p < 0.05$, $****p \leq 0.0001$.

(B) Motor axon degeneration in acute end-stage C9-BAC mice. Upper panel: axon size distribution in the ventral roots of the fourth lumbar section of the spinal cord (L4) from C9-BAC acute end-stage (red) and age-matched NT littermates (blue). Lower left panel: acute end-stage mice (red) show increased numbers of small axons (diameter $< 4 \mu\text{m}$) and decreased numbers of large axons (diameter $\geq 4 \mu\text{m}$) compared to NT animals (blue). Lower right panel: representative image of toluidine blue-stained L4 ventral roots. NT, $n = 5$; Acute, $n = 3$; mean \pm SD, unpaired t test, $*p < 0.05$, $**p \leq 0.01$, $***p \leq 0.001$.

(C) ChAT staining of motor neurons in the lumbar spinal cord. Left panel shows the IHC staining using ChAT antibody. Right panel shows decreased ChAT (+) motor neurons in acute end-stage compared to NT animals. NT, $n = 3$; Acute, $n = 3$; mean \pm SEM, unpaired t test, $**p \leq 0.01$.

(D) Vacuolated motor neurons visible with ChAT staining in acute end-stage animals.

(E) H & E stain showing degeneration of large pyramidal neurons in layer V of the motor cortex of acute end-stage animals.

in the cortex were found by CV staining in asymptomatic C9-500 and C9-500/32 mice at 2 or 5 months of age (Figure S6C).

Because pathological changes in the hippocampus have been reported in C9orf72 autopsy cases (Pletnikova et al., 2014), we looked at the hippocampal region in our mice using NeuN and CV staining. These experiments show dramatic loss of neurons in cornu ammonis (CA) and dentate gyrus (DG) regions of the hippocampus, with the patterns of neurodegeneration varying substantially between animals. Some animals showed marked degeneration of the CA1 region and others showed degeneration of the CA3 and DG, or the entire CA region (Figures 5C and S6D). These data are consistent with the variability of hippocampal neurodegeneration in human C9 (+) autopsy cases and the patchy accumulation of C9orf72 RAN proteins (Pletnikova et al., 2014; Zu et al., 2013).

Additionally, we examined the neuroinflammatory response that may be triggered in response to extensive neurodegenera-

tion. Acute end-stage mice show increased Iba1 staining of phagocytic microglia in the hippocampus compared to NT controls, suggesting this region is actively undergoing neurodegeneration at the time of death (Figures 5D and S6E). In addition, GFAP staining shows prominent astrocytosis in layers I–III and layer V of the motor cortex and the hippocampus compared to NT controls (Figures 5E, 5F, and S6F). These findings are consistent with reactive gliosis triggered in response to neurodegeneration.

Cerebellar atrophy has been reported both in autopsy tissue and through neuroimaging of patients with C9orf72 expansions (Mahoney et al., 2012; Whitwell et al., 2012). Examination of the cerebellum in acute end-stage mice shows a 65% loss of D28K-calbindin-positive Purkinje cells and a 28% decrease in thickness of the molecular layer compared to controls (Figures 6A–6C).

In addition to the ChAT-positive motor neurons (Figure 4C), NeuN- and CV-positive neurons in the lateral and posterior horns

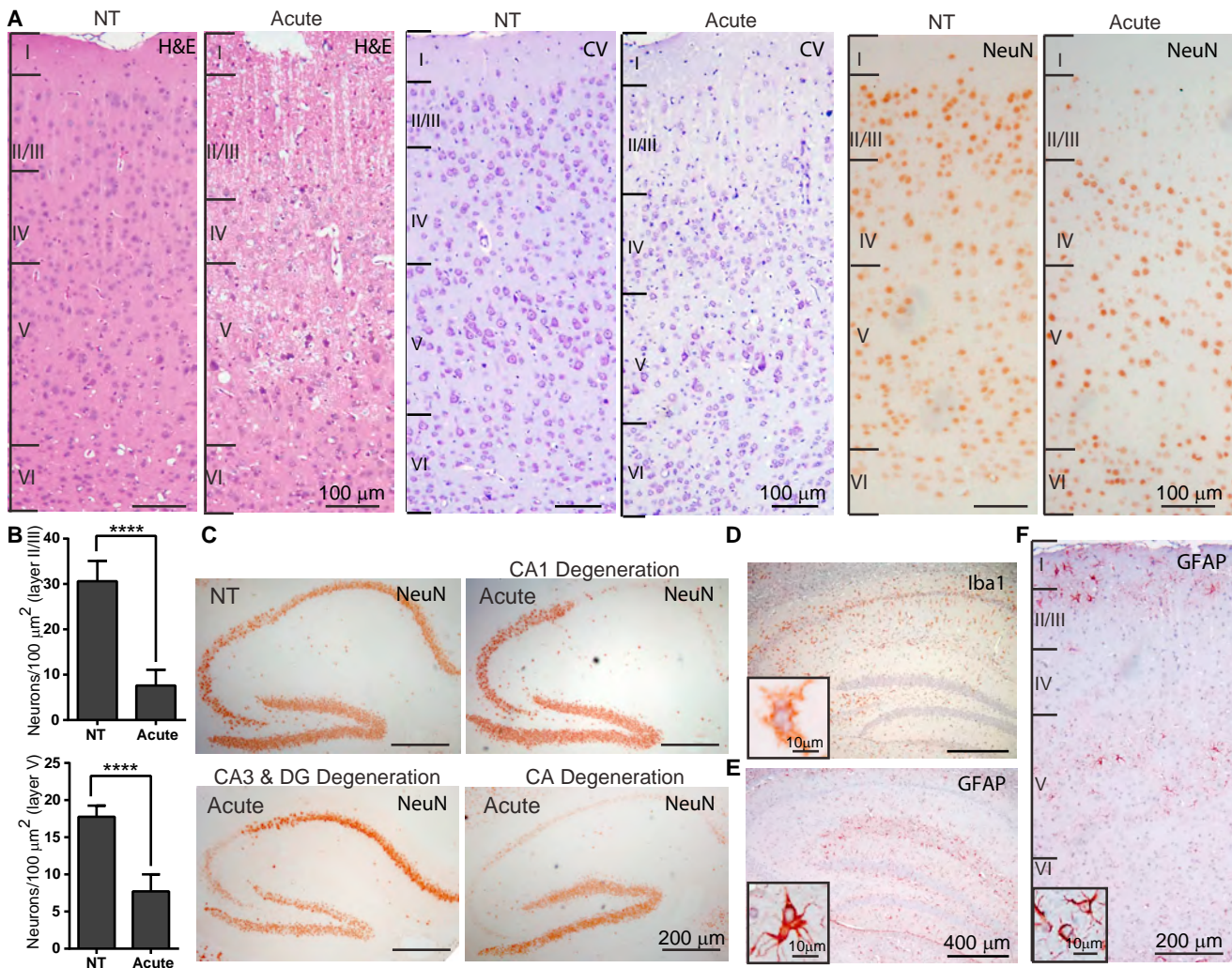


Figure 5. C9-BAC Mice Show Widespread Neurodegeneration in the Motor Cortex and Hippocampus

(A) H & E (left panel), CV (center panel), and IHC with NeuN antibody (right panel) of NT and acute end-stage animals showing neurodegeneration in layer II/III and layer V of the motor cortex.

(B) Quantification of neurons from CV-stained sections in layer II/III and layer V of the motor cortex shows extensive neurodegeneration. NT, n = 3; Acute, n = 3; mean \pm SEM, unpaired t test, ****p < 0.0001.

(C) NeuN staining shows variable patterns of hippocampal degeneration in C9-BAC acute end-stage mice.

(D) Iba1 staining shows microgliosis and macrophage activation in the degenerated CA1 region of the hippocampus. Inset: higher magnification of an activated microglia.

(E) GFAP staining shows astrocytosis in hippocampal white matter and DG region. Inset: higher magnification of a hypertrophic astrocyte.

(F) GFAP staining illustrating astrocytosis in layer I/II/III and layer V of motor cortex in an acute end-stage animal. Inset: higher magnification showing a reactive and hypertrophic astrocyte from layer V of the motor cortex.

of the spinal cord that predominantly contain interneurons were also decreased in the acute end-stage animals compared to NT controls (Figures 6D, 6E, and S6A), suggesting the possible involvement of these interneurons in disease.

In contrast to the acute end-stage animals, male and female mice with slowly progressive disease showed milder neurodegenerative changes. For example, at 18 months of age the slowly progressive animals showed focal rather than widespread degenerative changes in the neocortex, milder degenerative changes in the cerebellum, and no overt degeneration in the hippocampus (Figures S7A–S7D).

Taken together, these results indicate that acute end-stage C9-BAC mice have widespread neurodegenerative changes in the neocortex, hippocampus, cerebellum, and spinal cord. In contrast, the slowly progressive mice show loss of motor neurons in the spinal cord, focal sites of neurodegeneration in the neocortex, and milder degeneration of the cerebellum with relative sparing of the hippocampus.

C9-BAC Mice Show Molecular Hallmarks of ALS/FTD

Next, we tested if our BAC transgenic mice have hallmark molecular features of *C9orf72* ALS/FTD. We focused our analysis on

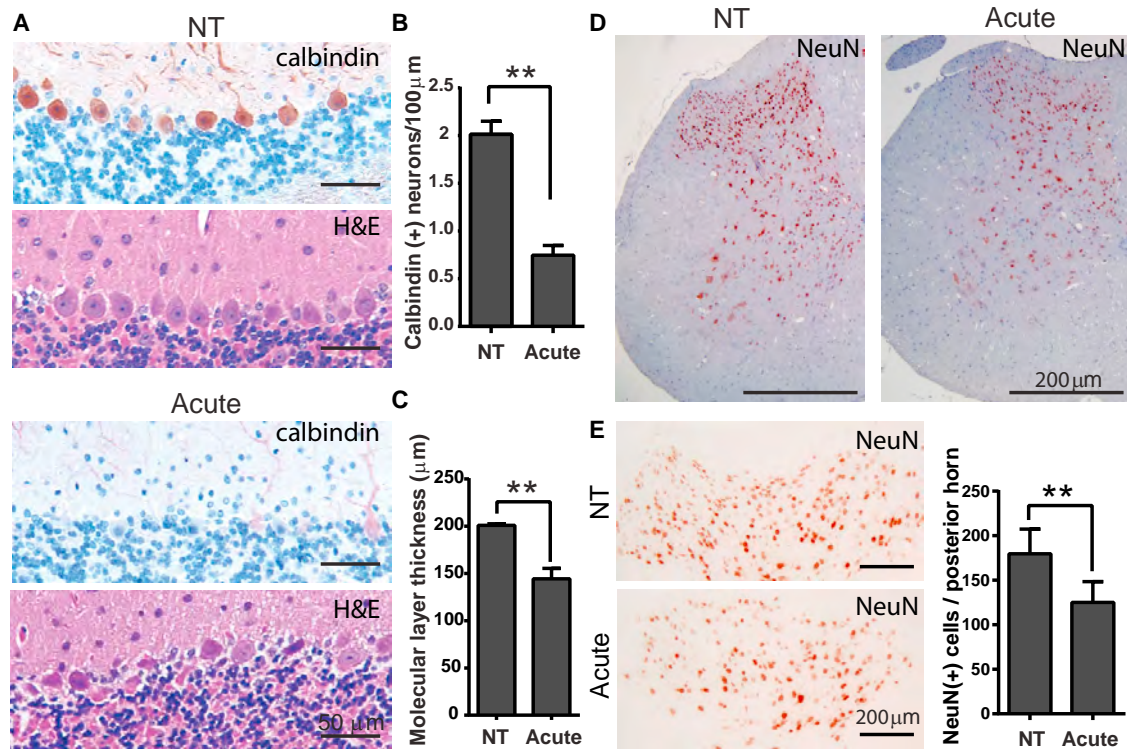


Figure 6. C9-BAC Mice Show Cerebellar and Interneuronal Loss in the CNS

(A) IHC with calbindin antibody and H & E staining show degeneration of cerebellar Purkinje cells.

(B) Quantification of calbindin-positive Purkinje cells. NT, n = 3; Acute, n = 3; mean ± SEM, unpaired t test, **p ≤ 0.01.

(C) Quantification of cerebellar molecular layer thickness. NT, n = 3; Acute, n = 3; mean ± SEM, unpaired t test, **p ≤ 0.01.

(D) NeuN staining counterstained with hematoxylin shows motor neuron (anterior horn) and interneuron (lateral and posterior horn) degeneration of the lumbar spinal cord.

(E) Interneuron degeneration in posterior horn of the spinal cord. Left panel: NeuN staining shows example of neuronal loss in posterior horn of C9-BAC acute end-stage animal compared to a NT littermate. Right panel: quantification of neuronal cells in posterior horn. NT, n = 3; Acute end-stage, n = 3; mean ± SEM, unpaired t test, **p ≤ 0.01.

the motor cortex, hippocampus, cerebellum, and spinal cord. We show by fluorescence in situ hybridization (FISH) that sense and antisense RNA foci accumulate in mice from the C9-500 and C9-500/32 lines as early as 2 months of age, but not in C9-36/29, C9-37, or NT controls (see examples in Figures 7A and S8). We used RNA foci in the long repeat lines as a marker of sense and antisense transcript distribution to begin to understand if sense or antisense transcripts or their corresponding RAN proteins are preferentially found in affected regions of the brain and spinal cord. Sense foci are found throughout the brain in nearly all NeuN-positive neuronal cells and also in a large portion of NeuN-negative cells (glia) in 2-month-old animals (Table 1). In contrast, antisense foci show a more specific pattern of accumulation in regions of the brain and spinal cord that degenerate. For example, abundant antisense foci are found in upper motor neurons in layer V of the motor cortex, CA and DG neurons in the hippocampus, and cerebellar Purkinje cells and interneurons in lateral and posterior horn of spinal cord. Moderate levels of antisense foci were found in layers II/III of the motor cortex and were occasionally seen in the layer IV of the motor cortex and the cerebellar granule and molecular layers. Different from sense foci,

antisense foci were not apparent in glia throughout the CNS or ChAT-positive motor neurons in the spinal cord (Figure S8; Table 1). No overt differences in sense and antisense RNA foci were observed in 2-month-old asymptomatic mice compared with acute end-stage mice (5–7 months) (Figures S8 and S9) or older slowly progressive mice (~18 months) (data not shown).

An additional hallmark of *C9orf72* ALS/FTD is the accumulation of RAN protein aggregates. In comparison to human autopsy tissue (Zu et al., 2013), detecting RAN protein aggregates in our mice was more challenging, possibly because the aggregates are smaller and have less time to develop during the shorter lifespan of mice. To improve RAN protein detection in our mice, we generated a novel monoclonal poly-GA antibody (27B11), which is highly specific for aggregated poly-GA protein (Figure S10). IHC staining using 27B11 shows small poly-GA aggregates throughout the brain in all three phenotypic lines (C9-500/32, C9-500, and C9-36/29), but not in NT controls (Figures 7B and S11A). In contrast, poly-GA aggregates were not detected in the C9-37 repeat line. Consistent with previous studies (Zu et al., 2011, 2013), these data indicate that increased repeat length favors RAN protein accumulation (C9-500 GA(+)) versus

C9-37 GA(-)) and also that repeats of ~36 are sufficient to trigger in vivo accumulation of RAN proteins if expression levels are sufficiently high (C9-36/29 GA(+)) versus C9-37 GA(-)). Additionally, we also detected poly-GP aggregates in the neocortex and thalamus of acute end-stage mice from the C9-500/32 and C9-500 lines (Figures 7C and S11B). To correlate RAN protein accumulation with disease, we compared poly-GA RAN protein aggregates in asymptomatic and symptomatic mice from the C9-500 line. In general, poly-GA RAN protein aggregates are abundant in acute end-stage and older mice but difficult to find in asymptomatic mice. Because the first region of the brain to show robust poly-GA accumulation is the retrosplenial cortex, we chose this region to correlate poly-GA RAN protein accumulation with age and disease status (Figure 7D). In asymptomatic animals at 2 months of age, poly-GA RAN protein aggregates in the retrosplenial cortex can be detected as infrequent, small, pin-like dots. At 5–7 months of age, asymptomatic mice have more pin-like poly-GA aggregates. In acute end-stage animals of the same age (5–7 months), the poly-GA aggregates are larger. Finally, in 18-month slow progressive mice, poly-GA aggregates are more abundant and larger (Figure 7D). These results demonstrate that the frequency and size of RAN protein aggregates increase with age and disease. The retrosplenial cortex was also positive for p62, a marker of autophagy (Figure S11C).

TDP-43 inclusions are a neuropathological feature found in >90% of ALS and 50% of FTD autopsy cases, including *C9orf72* ALS/FTD (Ling et al., 2013). TDP43 staining in our C9-BAC mice shows nuclear and cytoplasmic aggregates in degenerating neurons throughout the brain, including the hippocampus and levels II/III and V of the motor cortex (Figure 7E). These changes are found in the acute end-stage animals from the C9-500, C9-500/32, and C9-36/29 lines, but not in asymptomatic or control animals (Figure S11D).

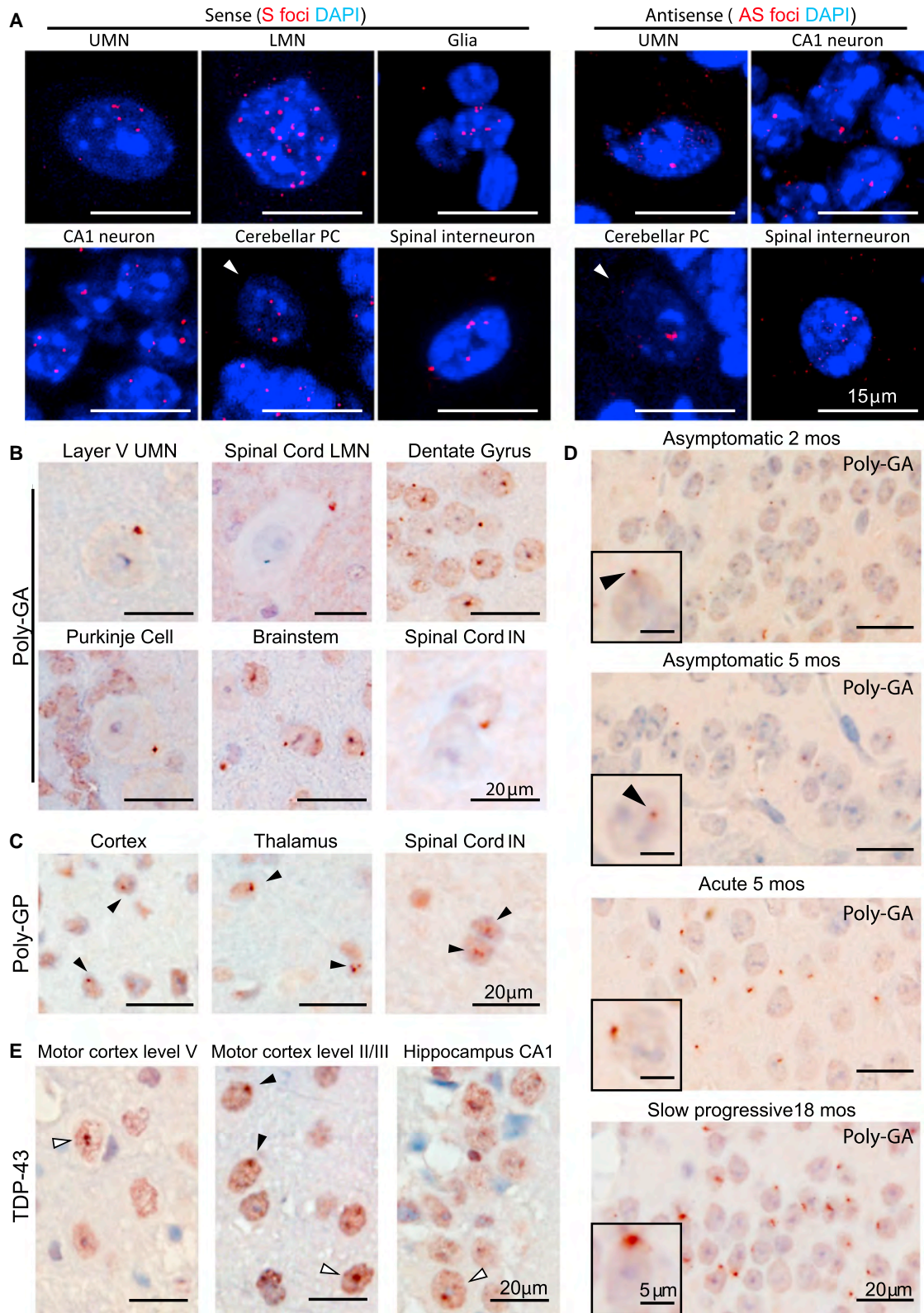
In summary, C9-BAC mice show C9 ALS/FTD hallmark molecular features of *C9orf72* ALS/FTD. Sense and antisense RNA foci accumulate in the brain and spinal cord in distinct patterns. RAN protein aggregate load increases with age and disease. TDP43 aggregation characteristic of ALS/FTD and other neurodegenerative diseases is found in acute end-stage C9-BAC mice.

DISCUSSION

We have developed a BAC transgenic model of *C9orf72* ALS/FTD in which the expression of the expansion mutation is driven by the endogenous human regulatory regions. Our model shows pleomorphic phenotypes including paralysis, anxiety-like behavior, decreased survival, and widespread neurodegeneration of the brain and spinal cord. Paralyzed mice showed degeneration of spinal motor neurons with significant cortical and hippocampal degeneration. Mice that do not develop the paralytic phenotype had less-severe degeneration in the brain and spinal cord. Similar to *C9orf72* patients (Zu et al., 2013), affected lines of mice show elevated antisense transcripts, RAN proteins, and TDP43 aggregates. These mice provide the first model that enables molecular dissection of the basis for clinically relevant phenotypes for *C9orf72* ALS and for testing the efficacy of therapeutic strategies.

Our C9-BAC mouse model provides insight into the mechanisms of *C9orf72* ALS/FTD. First, our finding that the human *C9orf72* containing BAC causes disease in a repeat-length and expression-dependent manner argues for gain-of-function and against loss-of-function mechanisms. These data are consistent with separate experiments showing the absence of typical disease phenotypes in *C9orf72* knockout mice (Koppers et al., 2015). Second, the phenotypes in our C9-36/29 line indicate that relatively short repeats, expressed at even moderately elevated levels, are sufficient to trigger disease. Although RNA foci are not present in the C9-36/29 mice, it is still possible that RNAs with moderate expansions sequester key RNA binding proteins and result in RNA processing abnormalities. Third, RAN protein accumulation correlates with disease severity in our C9-BAC mice. RAN proteins were found in all three phenotypic lines, including the C9-36/29, but not the C9-37, line. While these data suggest RAN protein accumulation may play an important role in disease, better antibodies and additional studies will be required to understand the role of sense and antisense RAN proteins in the disease onset and progression. Finally, the detection of TDP-43 pathology in acute end-stage mice mimics the TDP-43 aggregates present in *C9orf72* ALS/FTD patients and more than 90% of all ALS cases. Because TDP43 aggregates are only detected in highly degenerated regions in acute end-stage animals, it is not yet clear if TDP43 aggregation causes the degenerative changes or is a downstream result of neuronal degeneration. The development of interventions that target individual pathologies should allow for a better understanding of the time course of disease and events that mediate the different phenotypic aspects of our model.

Acute end-stage C9-BAC mice develop key neuropathological features of both ALS and FTD. Consistent with ALS, our mice show degeneration of the entire motor unit including neurons in the motor cortex and the lumbar spinal cord, ventral roots, and neuromuscular junctions of the TA and diaphragm. While degeneration of the ventral roots is statistically significant, the degeneration of the motor neurons and the denervation of the neuromuscular junctions are more dramatic. Given how quickly the acutely affected animals decline, it is possible that atrophied axons may linger for some period after the cell body and neuromuscular junction have degenerated, producing the data we observe. Pathological features of FTD include neurodegeneration of the hippocampus and pyramidal neurons of the frontal cortex (Kril and Halliday, 2011; Lashley et al., 2015). A typical feature of FTD is neuronal loss in layers II/III, which is often associated with mild to moderate spongiform changes and reactive gliosis (Seltman and Matthews, 2012; Thompson and Vinters, 2012). Similar to FTD patients, acute end-stage C9-BAC mice have striking neurodegeneration of cortical layers II/III, as well as the hippocampus, with widespread pyknotic nuclei, vacuolization, and gliosis. A recently appreciated feature of *C9orf72* ALS/FTD is cerebellar atrophy and pathology (Al-Sarraj et al., 2011; Gendron et al., 2015; Mahoney et al., 2012; Yokoyama and Rosen, 2012). Our mice also model this aspect of the disease and show Purkinje cell degeneration and thinning of the molecular layer. Cerebellar changes may underlie the gait abnormalities, one of the earliest phenotypes found in our mice. In summary, the neurodegenerative and neuroinflammatory



(legend on next page)

Table 1. Distribution Summary of Sense and Antisense RNA Foci in C9-BAC Lines with Long Repeats

Region	Cell Type	Sense Foci	Antisense Foci	Degeneration in Acute End-Stage Mice
Frontal cortex	Layer II/III neurons	++++	++	Y
	Layer IV neurons	++++	+	N
	Layer V neurons	++++	++++	Y
	Glia	++	–	N
Hippocampus	DG neurons	++++	++++	Y
	CA neurons	++++	++++	Y
Cerebellum	Purkinje cells	+++	++++	Y
	Granule cells	++++	+	N
	Glia	+++	–	N
Lumbar spinal cord	Lower motor neurons	++++	–	Y
	Interneurons	++++	++++	Y
	Glia	++	–	N

(–) no foci, (+) occasional foci, (++) moderate foci, (+++) numerous foci, (++++) abundant foci, (Y) degenerated at end stage, (N) not degenerated at end stage.

changes in our C9-BAC mice are consistent with the neuropathological features of the human disease and are likely to underlie the paralysis, respiratory dysfunction, and anxiety-like phenotypes found in our mice.

In contrast to the acute end-stage mice, animals with slow progressive phenotypes show only focal degeneration of the cortex, milder Purkinje cell loss, relative sparing of the hippocampus, and compensatory neuronal sprouting at the neuromuscular junctions. These milder neurodegenerative changes are consistent with the longer lifespan of the slow progressive animals compared to animals with acute disease.

Although the slow progressive disease phenotypes are fairly penetrant in males and females, the acute rapidly progressing phenotype was found in female, but not male mice. While we do not yet understand the molecular basis for this difference, hormonal regulation or sex-specific differences in inflammatory responses to RAN proteins may be contributing factors. Interestingly, a higher frequency of the more rapidly progressive, bulbar-onset ALS has been reported in female patients (63%) and in C9orf72 ALS (Cruts et al., 2013; Turner et al., 2010).

Bidirectional expression of expansion mutations is now a common theme in microsatellite expansion diseases (Batra et al., 2010; Cho et al., 2005; Moseley et al., 2006). Similar to the elevated levels of C9orf72 antisense transcripts seen in C9 (+) patient brains (Zu et al., 2013), antisense transcripts are also elevated in our expansion mice. The elevated levels of antisense expression in our C9-BAC mice (Figure 2E) suggest that the expansion mutation promotes antisense transcription, possibly by increasing chromatin accessibility to the transcriptional machinery.

Similar to C9orf72 autopsy cases (Cooper-Knock et al., 2015), sense and antisense foci show differences in distribution in brain and spinal cord in the C9-500 and C9-500/32 lines. Sense foci are widespread and abundant throughout the CNS and are found in regions of the brain that are susceptible and resistant to neurodegeneration. In contrast, antisense foci are primarily found in vulnerable regions of the CNS, including layers II/III and V of the cerebral cortex, the DG and CA regions of the hippocampus, and cerebellar Purkinje cell layer. A notable exception to this trend is in the spinal cord. Only sense foci were detected in motor neurons, while both sense and antisense foci were found in interneurons. Since both types of neurons degenerate, three possibilities arise: (1) motor neurons may be more susceptible to sense RNA than neurons in the rest of the CNS; (2) motor neurons in our mice express toxic antisense RNAs, but not the key RNA binding proteins required to sequester the antisense RNA into foci; and (3) antisense expression first affects the inhibitory interneurons, and loss of inhibitory input from the interneurons causes excitotoxicity and motor neuron death through a non-cell-autonomous process. Additionally, neurodegeneration of the interneurons containing antisense RNA indicates that the role of the interneurons in C9 ALS pathology may be underappreciated. These data and other evidence from cell culture and *Drosophila* models (Mizielinska et al., 2014; Wen et al., 2014) suggest that antisense transcripts and/or the corresponding antisense RAN proteins may be critical drivers of the disease.

In C9orf72 autopsy tissue, RAN proteins show a patchy and variable pattern of RAN protein accumulation (Pletnikova et al., 2014; Zu et al., 2013). In Huntington's disease, RAN protein accumulation occurs in a cell-type-specific manner, which is independent from the polyGln (Bañez-Coronel et al., 2015). In addition to cell-specific RNA gain-of-function mechanisms, it is possible that focal accumulation of one or more RAN proteins may underlie neurodegeneration, including the remarkably variable degenerative changes seen in the hippocampi of our mice.

Figure 7. C9-BAC Mice Exhibit Hallmark Features of C9 ALS/FTD with Sense and Antisense RNA Foci, RAN Protein Aggregates, and TDP-43 Pathology

(A) Sense and antisense RNA foci accumulate in the CNS of C9-BAC long repeat lines (C9-500 is shown here) from 2 months of age. Foci are labeled by FISH using Cy3-conjugated DNA probes (red), and nuclei are stained blue with DAPI. White arrows show cerebellar Purkinje cells.

(B) IHC staining with monoclonal poly-GA antibody (27B11) shows aggregates in C9-500 mouse brain and spinal cord neurons.

(C) IHC staining with poly-GP antibody (H3154) shows aggregates in C9-500 mouse brain and spinal cord neurons.

(D) Poly-GA accumulation in the C9-500 mice occurs in a time- and disease-dependent manner. Poly-GA aggregates in retrosplenial cortex of asymptomatic 2-month-old, asymptomatic 5-month-old, acute end-stage 5-month-old, and slow progressive 18-month-old mice from the C9-500 line. Higher magnification of a representative cell is shown as an inset in each image.

(E) Nuclear and cytoplasmic TDP-43 aggregates in the motor cortex and hippocampus of C9-BAC acute end-stage animals.

While further work is needed to understand the role of sense and antisense RNAs and RAN proteins in ALS/FTD, most therapeutic efforts for microsatellite expansion diseases have targeted the sense gene products (Hu et al., 2012; Kordasiewicz et al., 2012; Lagier-Tourenne et al., 2013; Wheeler et al., 2012). Since most of these diseases are late onset, therapeutic benefit may be achieved by targeting sense transcripts and lowering the burden of sense RNAs and RAN proteins. It is also possible that targeting the sense transcripts will lower or increase the steady-state levels of antisense transcripts (Sopher et al., 2011). An additional therapeutic approach would be to block the factors involved in RAN translation without affecting canonical translation.

Recently, two other groups reported the development of *C9orf72* BAC transgenic models (O'Rourke et al., 2015; Peters et al., 2015). Although these animals show sense and antisense RNA foci and the accumulation of the GP RAN protein, surprisingly, neither of these models developed phenotypic or neurodegenerative features of the disease. Possible explanations for this difference include (1) the absence of the full-length gene and 3' UTR regulatory region in one model (Peters et al., 2015); (2) differences in *cis* modifiers on the individual BAC transgenes; (3) differences in mouse genetic backgrounds, which have been previously reported to affect phenotypes in other neurodegenerative diseases (Hsiao et al., 1995; Strong et al., 2012); and (4) differences in transgene expression levels or spatial/temporal expression patterns. Detailed, side-by-side comparisons of these *C9orf72* BAC models may reveal new insight into ALS/FTD pathogenesis.

ALS and FTD are devastating and fatal neurodegenerative diseases. Efforts to develop therapeutic strategies have been hampered by the complexity of disease mechanisms. Our mice are the first to develop the molecular, behavioral, and neurodegenerative features of *C9orf72* ALS/FTD. Antisense transcripts in these mice are upregulated and preferentially accumulate in cell populations vulnerable to neurodegeneration. Additionally, RAN protein accumulation increases with age and disease severity. Taken together, these data support a model in which antisense transcripts and/or RAN proteins are critical drivers of disease pathogenesis. These mice provide an important tool that can be used to tease apart the most important molecular mechanisms of this complex disease and test the efficacy of therapeutic strategies, not just by reversing one or more molecular markers of disease, but by reversing the disease itself.

EXPERIMENTAL PROCEDURES

A BAC library from a patient-derived LCL was generated. BAC clones were screened by DNA dot blot analysis with a DNA probe targeting the *C9orf72* gene. Four BAC transgenic lines were established after pronuclear injection. Molecular studies including southern blot, PCR, repeat-primed PCR, and qRT-PCR were performed to characterize transgene copy number and sense and antisense expression levels. Gait analyses, grip strength, cage behavior, and open field testing were done to look for ALS and FTD phenotypes. Histological analyses included assessment of neuromuscular junctions in the tibialis and diaphragm muscles, quantification of motor neuron ventral roots, and immunohistochemistry of the brain and spinal cord using a variety of antibodies. Assessment of RNA foci and colocalization with neurons (Neu-N) in the brain or lower motor neurons (ChAT) in the spinal cord were performed. See Supplemental Experimental Procedures for additional details.

SUPPLEMENTAL INFORMATION

Supplemental Information includes Supplemental Experimental Procedures, eleven figures, two tables, and three movies and can be found with this article online at <http://dx.doi.org/10.1016/j.neuron.2016.04.005>.

AUTHOR CONTRIBUTIONS

Y.L., A.P., and L.P.W.R. designed research; Y.L., A.P., T.Z., T.R., and O.B. performed research; D.R.B. contributed new reagents, analytic tools, and samples; Y.L., A.P., T.Z., T.R., D.R.B., A.T.Y., and L.P.W.R. analyzed data; and Y.L., A.P., and L.P.W.R. wrote the paper with input from all authors.

ACKNOWLEDGMENTS

We would like to thank the ALS family members who contributed DNA to this study; Dr. M. Swanson, Dr. J.D. Cleary, and all the members of the L.P.W.R. lab for helpful discussions and suggestions; Dr. Y. Qiu for providing cell lines and plasmids for the baculovirus expression system; Dr. K. Braunstein and Dr. P. Wong; Johns Hopkins University for technical input for spinal root quantification; Dr. L. Notterpek, Dr. D. Falk, and Dr. M. Swanson for their technical help on staining and characterization of neuromuscular junctions; Dr. S.H. Subramony for his help on analyzing muscle immunohistochemistry; and Dr. T. Hathorn for help with behavioral analyses. This work was funded by Target ALS, the ALS Association, the Robert Packard Center for ALS Research, start-up funding from the University of Florida (L.P.W.R.), and support from the Santa-Fe HealthCare Alzheimer's Disease Research Center (D.R.B.). T.Z. and L.P.W.R. have patents pending on RAN translation.

Received: December 21, 2015

Revised: March 1, 2016

Accepted: March 29, 2016

Published: April 21, 2016

REFERENCES

- Al-Sarraj, S., King, A., Troakes, C., Smith, B., Maekawa, S., Bodi, I., Rogelj, B., Al-Chalabi, A., Hortobágyi, T., and Shaw, C.E. (2011). p62 positive, TDP-43 negative, neuronal cytoplasmic and intranuclear inclusions in the cerebellum and hippocampus define the pathology of *C9orf72*-linked FTL and MND/ALS. *Acta Neuropathol.* 122, 691–702.
- Ash, P.E., Bieniek, K.F., Gendron, T.F., Caulfield, T., Lin, W.L., DeJesus-Hernandez, M., van Blitterswijk, M.M., Jansen-West, K., Paul, J.W., 3rd, Rademakers, R., et al. (2013). Unconventional translation of *C9ORF72* GGGGCC expansion generates insoluble polypeptides specific to c9FTD/ALS. *Neuron* 77, 639–646.
- Bañez-Coronel, M., Ayhan, F., Tarabochia, A.D., Zu, T., Perez, B.A., Tusi, S.K., Pletnikova, O., Borchelt, D.R., Ross, C.A., Margolis, R.L., et al. (2015). RAN translation in Huntington disease. *Neuron* 88, 667–677.
- Batra, R., Charizanis, K., and Swanson, M.S. (2010). Partners in crime: bidirectional transcription in unstable microsatellite disease. *Hum. Mol. Genet.* 19 (R1), R77–R82.
- Chew, J., Gendron, T.F., Prudencio, M., Sasaguri, H., Zhang, Y.J., Castanedes-Casey, M., Lee, C.W., Jansen-West, K., Kurti, A., Murray, M.E., et al. (2015). Neurodegeneration. *C9ORF72* repeat expansions in mice cause TDP-43 pathology, neuronal loss, and behavioral deficits. *Science* 348, 1151–1154.
- Cho, D.H., Thienes, C.P., Mahoney, S.E., Analau, E., Filippova, G.N., and Tapscott, S.J. (2005). Antisense transcription and heterochromatin at the DM1 CTG repeats are constrained by CTCF. *Mol. Cell* 20, 483–489.
- Ciura, S., Lattante, S., Le Ber, I., Latouche, M., Tostivint, H., Brice, A., and Kabashi, E. (2013). Loss of function of *C9orf72* causes motor deficits in a zebrafish model of amyotrophic lateral sclerosis. *Ann. Neurol.* 74, 180–187.
- Cleary, J.D., and Ranum, L.P. (2013). Repeat-associated non-ATG (RAN) translation in neurological disease. *Hum. Mol. Genet.* 22 (R1), R45–R51.

- Cleary, J.D., and Ranum, L.P. (2014). Repeat associated non-ATG (RAN) translation: new starts in microsatellite expansion disorders. *Curr. Opin. Genet. Dev.* **26**, 6–15.
- Cooper-Knock, J., Higginbottom, A., Stopford, M.J., Highley, J.R., Ince, P.G., Wharton, S.B., Pickering-Brown, S., Kirby, J., Hautbergue, G.M., and Shaw, P.J. (2015). Antisense RNA foci in the motor neurons of C9ORF72-ALS patients are associated with TDP-43 proteinopathy. *Acta Neuropathol.* **130**, 63–75.
- Cruts, M., Gijselinck, I., Van Langenhove, T., van der Zee, J., and Van Broeckhoven, C. (2013). Current insights into the C9orf72 repeat expansion diseases of the FTL/ALS spectrum. *Trends Neurosci.* **36**, 450–459.
- DeJesus-Hernandez, M., Mackenzie, I.R., Boeve, B.F., Boxer, A.L., Baker, M., Rutherford, N.J., Nicholson, A.M., Finch, N.A., Flynn, H., Adamson, J., et al. (2011). Expanded GGGGCC hexanucleotide repeat in noncoding region of C9ORF72 causes chromosome 9p-linked FTD and ALS. *Neuron* **72**, 245–256.
- Freibaum, B.D., Lu, Y., Lopez-Gonzalez, R., Kim, N.C., Almeida, S., Lee, K.H., Badders, N., Valentine, M., Miller, B.L., Wong, P.C., et al. (2015). GGGGCC repeat expansion in C9orf72 compromises nucleocytoplasmic transport. *Nature* **525**, 129–133.
- Gendron, T.F., van Blitterswijk, M., Bieniek, K.F., Daugherty, L.M., Jiang, J., Rush, B.K., Pedraza, O., Lucas, J.A., Murray, M.E., Desaro, P., et al. (2015). Cerebellar c9RAN proteins associate with clinical and neuropathological characteristics of C9ORF72 repeat expansion carriers. *Acta Neuropathol.* **130**, 559–573.
- Goodwin, M., and Swanson, M.S. (2014). RNA-binding protein misregulation in microsatellite expansion disorders. *Adv. Exp. Med. Biol.* **825**, 353–388.
- Hsiao, K.K., Borchelt, D.R., Olson, K., Johannsdottir, R., Kitt, C., Yunis, W., Xu, S., Eckman, C., Younkin, S., Price, D., et al. (1995). Age-related CNS disorder and early death in transgenic FVB/N mice overexpressing Alzheimer amyloid precursor proteins. *Neuron* **15**, 1203–1218.
- Hu, J., Liu, J., Yu, D., Chu, Y., and Corey, D.R. (2012). Mechanism of allele-selective inhibition of huntingtin expression by duplex RNAs that target CAG repeats: function through the RNAi pathway. *Nucleic Acids Res.* **40**, 11270–11280.
- Jovičić, A., Mertens, J., Boeynaems, S., Bogaert, E., Chai, N., Yamada, S.B., Paul, J.W., 3rd, Sun, S., Herdy, J.R., Bieri, G., et al. (2015). Modifiers of C9orf72 dipeptide repeat toxicity connect nucleocytoplasmic transport defects to FTD/ALS. *Nat. Neurosci.* **18**, 1226–1229.
- Keum, S., Park, J., Kim, A., Park, J., Kim, K.K., Jeong, J., and Shin, H.S. (2016). Variability in empathic fear response among 11 inbred strains of mice. *Genes Brain Behav.* **15**, 231–242.
- Koppers, M., Blokhuis, A.M., Westeneng, H.J., Terpstra, M.L., Zundel, C.A., Vieira de Sá, R., Schellevis, R.D., Waite, A.J., Blake, D.J., Veldink, J.H., et al. (2015). C9orf72 ablation in mice does not cause motor neuron degeneration or motor deficits. *Ann. Neurol.* **78**, 426–438.
- Kordasiewicz, H.B., Stanek, L.M., Wancewicz, E.V., Mazur, C., McAlonis, M.M., Pytel, K.A., Artates, J.W., Weiss, A., Cheng, S.H., Shihabuddin, L.S., et al. (2012). Sustained therapeutic reversal of Huntington's disease by transient repression of huntingtin synthesis. *Neuron* **74**, 1031–1044.
- Kril, J.J., and Halliday, G.M. (2011). Pathological staging of frontotemporal lobar degeneration. *J. Mol. Neurosci.* **45**, 379–383.
- Kwon, I., Xiang, S., Kato, M., Wu, L., Theodoropoulos, P., Wang, T., Kim, J., Yun, J., Xie, Y., and McKnight, S.L. (2014). Poly-dipeptides encoded by the C9orf72 repeats bind nucleoli, impede RNA biogenesis, and kill cells. *Science* **345**, 1139–1145.
- Lagier-Tourenne, C., Baughn, M., Rigo, F., Sun, S., Liu, P., Li, H.R., Jiang, J., Watt, A.T., Chun, S., Katz, M., et al. (2013). Targeted degradation of sense and antisense C9orf72 RNA foci as therapy for ALS and frontotemporal degeneration. *Proc. Natl. Acad. Sci. USA* **110**, E4530–E4539.
- Lashley, T., Rohrer, J.D., Mead, S., and Revesz, T. (2015). Review: an update on clinical, genetic and pathological aspects of frontotemporal lobar degenerations. *Neuropathol. Appl. Neurobiol.* **41**, 858–881.
- Ling, S.C., Polymenidou, M., and Cleveland, D.W. (2013). Converging mechanisms in ALS and FTD: disrupted RNA and protein homeostasis. *Neuron* **79**, 416–438.
- Mahoney, C.J., Beck, J., Rohrer, J.D., Lashley, T., Mok, K., Shakespeare, T., Yeatman, T., Warrington, E.K., Schott, J.M., Fox, N.C., et al. (2012). Frontotemporal dementia with the C9ORF72 hexanucleotide repeat expansion: clinical, neuroanatomical and neuropathological features. *Brain* **135**, 736–750.
- McKhann, G.M., Albert, M.S., Grossman, M., Miller, B., Dickson, D., and Trojanowski, J.Q.; Work Group on Frontotemporal Dementia and Pick's Disease (2001). Clinical and pathological diagnosis of frontotemporal dementia: report of the Work Group on Frontotemporal Dementia and Pick's Disease. *Arch. Neurol.* **58**, 1803–1809.
- Miller, B.H., Schultz, L.E., Gulati, A., Su, A.I., and Pletcher, M.T. (2010). Phenotypic characterization of a genetically diverse panel of mice for behavioral despair and anxiety. *PLoS ONE* **5**, e14458.
- Milner, L.C., and Crabbe, J.C. (2008). Three murine anxiety models: results from multiple inbred strain comparisons. *Genes Brain Behav.* **7**, 496–505.
- Mizielinska, S., Grönke, S., Niccoli, T., Ridler, C.E., Clayton, E.L., Devoy, A., Moens, T., Norona, F.E., Woollacott, I.O., Pietrzyk, J., et al. (2014). C9orf72 repeat expansions cause neurodegeneration in *Drosophila* through arginine-rich proteins. *Science* **345**, 1192–1194.
- Mori, K., Weng, S.M., Arzberger, T., May, S., Rentzsch, K., Kremmer, E., Schmid, B., Kretschmar, H.A., Cruts, M., Van Broeckhoven, C., et al. (2013). The C9orf72 GGGGCC repeat is translated into aggregating dipeptide-repeat proteins in FTD/ALS. *Science* **339**, 1335–1338.
- Moseley, M.L., Zu, T., Ikeda, Y., Gao, W., Mosemiller, A.K., Daughters, R.S., Chen, G., Weatherspoon, M.R., Clark, H.B., Ebner, T.J., et al. (2006). Bidirectional expression of CUG and CAG expansion transcripts and intranuclear polyglutamine inclusions in spinocerebellar ataxia type 8. *Nat. Genet.* **38**, 758–769.
- O'Rourke, J.G., Bogdanik, L., Muhammad, A.K.M.G., Gendron, T.F., Kim, K.J., Austin, A., Cady, J., Liu, E.Y., Zarrow, J., Grant, S., et al. (2015). C9orf72 BAC transgenic mice display typical pathologic features of ALS/FTD. *Neuron* **88**, 892–901.
- Orr, H.T., and Zoghbi, H.Y. (2007). Trinucleotide repeat disorders. *Annu. Rev. Neurosci.* **30**, 575–621.
- Peters, O.M., Cabrera, G.T., Tran, H., Gendron, T.F., McKeon, J.E., Metterville, J., Weiss, A., Wightman, N., Salameh, J., Kim, J., et al. (2015). Human C9ORF72 hexanucleotide expansion reproduces RNA foci and dipeptide repeat proteins but not neurodegeneration in BAC transgenic mice. *Neuron* **88**, 902–909.
- Pletnikova, O., Sloane, K.L., Renton, A.E., Traynor, B.J., Crain, B.J., Reid, T., Zu, T., Ranum, L.P., Troncoso, J.C., Rabins, P.V., and Onyke, C.U. (2014). Hippocampal sclerosis dementia with the C9ORF72 hexanucleotide repeat expansion. *Neurobiol. Aging* **35**, 2419.e17–2419.e21.
- Ranum, L.P., and Cooper, T.A. (2006). RNA-mediated neuromuscular disorders. *Annu. Rev. Neurosci.* **29**, 259–277.
- Renton, A.E., Majounie, E., Waite, A., Simón-Sánchez, J., Rollinson, S., Gibbs, J.R., Schymick, J.C., Laaksovirta, H., van Swieten, J.C., Myllykangas, L., et al.; ITALSGEN Consortium (2011). A hexanucleotide repeat expansion in C9ORF72 is the cause of chromosome 9p21-linked ALS-FTD. *Neuron* **72**, 257–268.
- Rowland, L.P., and Shneider, N.A. (2001). Amyotrophic lateral sclerosis. *N. Engl. J. Med.* **344**, 1688–1700.
- Seltman, R.E., and Matthews, B.R. (2012). Frontotemporal lobar degeneration: epidemiology, pathology, diagnosis and management. *CNS Drugs* **26**, 841–870.
- Sopher, B.L., Ladd, P.D., Pineda, V.V., Libby, R.T., Sunkin, S.M., Hurley, J.B., Thienes, C.P., Gaasterland, T., Filippova, G.N., and La Spada, A.R. (2011). CTCF regulates ataxin-7 expression through promotion of a convergently transcribed, antisense noncoding RNA. *Neuron* **70**, 1071–1084.

- Strong, M.K., Southwell, A.L., Yonan, J.M., Hayden, M.R., Macgregor, G.R., Thompson, L.M., and Steward, O. (2012). Age-dependent resistance to excitotoxicity in Htt CAG140 mice and the effect of strain background. *J. Huntingtons Dis.* *1*, 221–241.
- Suzuki, N., Maroof, A.M., Merkle, F.T., Koszka, K., Intoh, A., Armstrong, I., Moccia, R., Davis-Dusenbery, B.N., and Eggan, K. (2013). The mouse C9ORF72 ortholog is enriched in neurons known to degenerate in ALS and FTD. *Nat. Neurosci.* *16*, 1725–1727.
- Therrien, M., Rouleau, G.A., Dion, P.A., and Parker, J.A. (2013). Deletion of C9ORF72 results in motor neuron degeneration and stress sensitivity in *C. elegans*. *PLoS ONE* *8*, e83450.
- Thompson, P.M., and Vinters, H.V. (2012). Pathologic lesions in neurodegenerative disease. In *Molecular Biology of Neurodegenerative Diseases D*, B. Teplow, ed. (Elsevier), pp. 1–33.
- Turner, M.R., Scaber, J., Goodfellow, J.A., Lord, M.E., Marsden, R., and Talbot, K. (2010). The diagnostic pathway and prognosis in bulbar-onset amyotrophic lateral sclerosis. *J. Neurol. Sci.* *294*, 81–85.
- Wen, X., Tan, W., Westergard, T., Krishnamurthy, K., Markandiah, S.S., Shi, Y., Lin, S., Shneider, N.A., Monaghan, J., Pandey, U.B., et al. (2014). Antisense proline-arginine RAN dipeptides linked to C9ORF72-ALS/FTD form toxic nuclear aggregates that initiate in vitro and in vivo neuronal death. *Neuron* *84*, 1213–1225.
- Wheeler, T.M., Leger, A.J., Pandey, S.K., MacLeod, A.R., Nakamori, M., Cheng, S.H., Wentworth, B.M., Bennett, C.F., and Thornton, C.A. (2012). Targeting nuclear RNA for in vivo correction of myotonic dystrophy. *Nature* *488*, 111–115.
- Whitwell, J.L., Weigand, S.D., Boeve, B.F., Senjem, M.L., Gunter, J.L., DeJesus-Hernandez, M., Rutherford, N.J., Baker, M., Knopman, D.S., Wszolek, Z.K., et al. (2012). Neuroimaging signatures of frontotemporal dementia genetics: C9ORF72, tau, progranulin and sporadics. *Brain* *135*, 794–806.
- Yokoyama, J.S., and Rosen, H.J. (2012). Neuroimaging features of C9ORF72 expansion. *Alzheimers Res. Ther.* *4*, 45.
- Zhang, K., Donnelly, C.J., Haeusler, A.R., Grima, J.C., Machamer, J.B., Steinwald, P., Daley, E.L., Miller, S.J., Cunningham, K.M., Vidensky, S., et al. (2015). The C9orf72 repeat expansion disrupts nucleocytoplasmic transport. *Nature* *525*, 56–61.
- Zu, T., Gibbens, B., Doty, N.S., Gomes-Pereira, M., Huguet, A., Stone, M.D., Margolis, J., Peterson, M., Markowski, T.W., Ingram, M.A., et al. (2011). Non-ATG-initiated translation directed by microsatellite expansions. *Proc. Natl. Acad. Sci. USA* *108*, 260–265.
- Zu, T., Liu, Y., Bañez-Coronel, M., Reid, T., Pletnikova, O., Lewis, J., Miller, T.M., Harms, M.B., Falchook, A.E., Subramony, S.H., et al. (2013). RAN proteins and RNA foci from antisense transcripts in C9ORF72 ALS and frontotemporal dementia. *Proc. Natl. Acad. Sci. USA* *110*, E4968–E4977.

Neuron, Volume 90

Supplemental Information

***C9orf72* BAC Mouse Model with Motor Deficits
and Neurodegenerative Features of ALS/FTD**

Yuanjing Liu, Amrutha Pattamatta, Tao Zu, Tammy Reid, Olgert Bardhi, David R. Borchelt, Anthony T. Yachnis, and Laura P.W. Ranum

Supplemental Experimental Procedures

Human Lymphoblastoid Cells. *C9orf72* ALS/FTD patient blood was collected with informed consent as approved by the local institutional review boards (IRB) at the University of Minnesota and the University of Florida and lymphoblastoid cell lines were established using standard methods.

Transgene construct and generation of BAC transgenic mice. A BAC library from a patient derived lymphoblastoid cell line (LCL) with approximately 1200 repeats was generated by Amplicon Express. HindIII was used to partially digest the patient genomic DNA and the fragments were cloned into the pCC1BAC vector. 39,936 clones with an average insert size of 110kb were picked. BAC clones were screened by DNA dot blot analysis with a DNA probe targeting the *C9orf72* gene PCR, generated by PCR using primer set Probe-F and -R (Table S1). C9 positive clones were expanded on a small scale and BAC DNA was extracted using BACMAX™ DNA purification kit (Epicenter). The length of the *C9orf72* G4C2 expansion was determined by Southern blotting. Expansion positive clones were sequenced using the pCC1-F and -R primers (Table S1) to identify the 5' and 3' ends of the insertion. Clone 002:B7 was shown to contain a 98kb insert from Chromosome 9 (27,527,137 bp to 27,625,470 bp) (Human Genome Feb. 2009 GRCh37/hg19) with *C9orf72* containing 52 kb of upstream sequence and 19.4 kb of downstream sequence. This BAC contains 2kb of the nearby *Mps one binder kinase activator 3B (MOB3B)* gene but not the ATG initiation site for the *MOB3B* open reading frame (ORF) nor any portion of the neighboring *interferon kappa, IFNK* gene.

Because the G4C2 repeat expansion is highly unstable in bacteria, we used a modified strategy to grow the bacteria to maximize the likelihood of retaining the expansion mutation. First, we streaked out the bacteria on plates and selected colonies of various sizes (small, medium and large), diluted them in liquid media and then plated each individual culture as a lawn of bacteria on agarose luria broth (LB) plates with 12.5 µg/ml chloramphenicol, at 25 °C or 30 °C in order to prevent possible overgrowth if repeat contractions result in faster growth. Five 25cm LB agarose plates were plated for each subclone in each condition, two subclones, s3-25 and m5-30 with the biggest expansions (830 or more repeats) were chosen for large-scale DNA extraction (QIAGEN). Both BAC DNAs were further purified using 0.05µm dialysis filters and subjected to pronuclear microinjection into fertilized mouse eggs with an FVB/NJ background at a concentration of 2ng/µl. The microinjections were performed by the transgenic mouse facility at the University of Florida. Animal studies were approved by the Institutional Animal Care and Use Committee at University of Florida. Founders and positive off-spring were identified by PCR analysis of tail DNA using NEB Quik-Load Taq Mastermix with transgene-specific primers C9GT-F and -R (Table S1) with an initial denaturation at 94 °C for 3 min, then 32 cycles (94 °C for 45s, 55 °C for 45s, 72 °C for 1 min), followed by a final elongation at 72 °C for 6 min.

Southern blot. A 241bp DNA probe was generated by PCR using primer set Probe-F and -R (Table S1) using a construct with human *C9orf72* DNA fragments as template. With an initial denaturation at 94 °C for 3 min, then 32 cycles (94 °C for 45s, 58 °C for 45s, 72 °C for 1 min), followed by a final elongation at 72 °C for 6 min. α -³²P-dCTPs were incorporated into 25ng of the DNA probe using Random Primed DNA labeling kit (Invitrogen), purified with ProbeQuant™ G-50 Micro columns (GE Healthcare) and denatured at 100 °C in boiling water. A total of 5µg (BAC DNA)-12 µg (human or mouse gDNA) was digested with XbaI (for human gDNA and BAC DNA) or EcoRI and BamHI (for mouse DNA) at 37 °C over night and electrophoresed in 0.9% agarose gels in 1×TAE. The agarose gels were depurinated in 0.1N HCl, denatured in 1.5M NaCl, 0.5M NaOH and neutralized in 1.5M NaCl, 0.5M Tris HCl pH 7.5 for 15 min at each step. DNA was transferred to a positively charged nylon membrane (GE Healthcare) by capillary blotting and crosslinked by UV irradiation. After two hours of prehybridization with Amersham™ Rapid-hyb buffer (GE Healthcare), the membrane was then hybridized with the probe for 3 hours at 65 °C in a rotating hybridization oven. The membrane was then washed once with 2×SSC, 0.1% SDS solution at room temperature for 20mins and two times with 0.2×SSC, 0.1% SDS solution at 65 °C for 15 min per wash. Radioactive signal was visualized on X-ray film after 2 days of exposure at -80 °C

Repeat-primed PCR and fragment assay. Repeat-primed PCR and fragment assay were performed as described in (1). FAM labeled PCR products were analyzed on an ABI3730 DNA analyzer (Applied

Biosystems) and data was analyzed using GeneMarkers software (version 1.75, SoftGenetics) at University of Florida Interdisciplinary Center for Biotechnology Research.

Real time RT-PCR. Total RNA was isolated from mouse frontal cortex and spinal cord tissues with TRIzol (Invitrogen). DNA contamination was eliminated by DNase I (Ambion) treatment at 37°C for 30 min and followed by heat inactivation at 75°C for 10min. Total RNA was reverse-transcribed using SuperScript III RT kit (Invitrogen) and random-hexamer primers (Applied Biosystems). Using strand specific RT PCR we previously identified primer pairs that only amplify sense or antisense *C9orf72* transcripts (2). After carefully confirming the strand specificity of these primers in our transgenic mice we used the following primers to detect sense and antisense transcripts: *C9orf72* mRNA (primer set C9mRNA-F and -R), *C9orf72* Exon 1a (primer set 1a-F and -R), antisense RNA (ASORF F and -R), mouse *C9orf72* ortholog (primer set mC9-F and -R) and mouse β -actin (primer set mACT-F and -R) in the same cDNA, so the relative expression level normalized by β -actin of each transcript is more reliable. Two-step quantitative RT-PCR was performed on a MyCycler Thermal Cycler system (Bio-Rad) using SYBR Green PCR Master Mix (Bio-Rad) and Gene specific primer sets [95°C 3min, 40 cycles (95 °C 30 s, 60 °C 30 s), 95°C 1min, 60°C 1min. Melting curve was performed [71 cycles (60°C - 95°C 10s per cycles)] in an optical 96-well plate with triplicates of each sample cDNA/primer pair for n=3-4 animals per line for each experiment. (see primer sequence in Table S2).

Gait analysis. Digital video images of the underside of the mouse were collected with a high-speed video camera from below the transparent belt of a motorized treadmill (DigiGait™ Imaging system, Mouse Specific). C9-BAC mice and their littermates were tested at 4 months of age. Each mouse was allowed to explore the treadmill compartment with the motor speed set to 14cm/s for 1min, then the motor speed was increased to 24cm/s for video recording. Only video recordings in which the mouse walked straight ahead with a constant relative position with respect to the camera were used for analysis. Data from each paw was analyzed with DigiGait automated gait analysis software (Mouse Specifics).

Grip strength. Grip strength was measured using a grip strength monitor (Columbus Instruments). Each mouse was held 2 cm away from the base of its tail near the wire mesh pull-bar assembly and all four paws were allowed to grasp the assembly. The mouse was then gradually drawn away from the assembly until the pull-bar was released. The highest force generated by pulling the animals away three times from the wire mesh was recorded. Three overall trials were performed for each animal.

Open field analysis. Open field analysis was performed by testing mouse behavior during a 30 min session in a completely dark open chamber (17"×17") (Med Associates). Approximately two hours before the start of analysis, mice were placed in the testing room to allow for acclimation to the room. Mice were then placed in the center of the darkened activity-monitoring chamber. The trace path and center time was recorded and analyzed with Activity Monitor (MED associates, Inc.) software.

Neuromuscular junction analysis. Acute onset end-stage animals and age-matched littermates were perfused transcardially with phosphate buffered saline (PBS). Diaphragm and tibialis anterior (TA) muscles were dissected and fixed in 1% paraformaldehyde (PFA) at 4°C overnight. The next day myofibers were teased apart into 10-20 thin muscle bundles (5 to 20 fibers per bundle). Acetylcholine receptors in neuromuscular junctions were stained with 1 μ g/ml α -bungarotoxin, tetramethylrhodamine conjugate (T1175, Invitrogen). Motor axons and synapses were stained with neurofilament H antibody (CPCA-NF-H, EnCor Biotechnology, 1:2000 dilution), rinsed 3 times in PBS with 0.05% Triton-X100 for 1 hour each and then stained using a secondary α -chicken antibody conjugated with Alexa Fluor 488 (IgG H+L Invitrogen 1:2000 dilution). Confocal images were taken at 20 \times magnification with 1 μ m between stacks for each muscle bundle. The percentage of NMJs (n=100) that were innervated were analyzed and plotted. Scoring was done in a blinded fashion.

All studies were done in a blinded fashion and scored by two independent investigators. Technical artifacts such as stripping of the section during tissue preparation are unlikely because fibers from a single muscle were processed together and there were always muscles that were still enervated on every slide. Additionally, three animals from each group were analyzed and muscles from both right and left legs were used and all muscles from the affected animals showed substantially differences from controls.

Ventral Root Quantification. Mice were perfused transcardially with phosphate buffer and followed by 4% paraformaldehyde in phosphate buffer. L4 ventral spinal roots were excised and post-fixed in 1% glutaraldehyde, 4% paraformaldehyde in phosphate buffer. The tissue was then embedded in Epon plastic and 1- μ m-thick cross-sections were cut on an ultramicrotome, stained with toluidine blue, rinsed, and cover-slipped in the electron microscopy core facility at University of Florida. Images were captured with an Olympus BX51 microscope and the axon areas were measured using ImageJ software (National Institutes of Health), individual axon diameters were calculated from the area measurements of individual axons.

Fluorescence in situ hybridization (FISH) with immunofluorescence (IF). Mice were perfused transcardially with PBS. Brain and lumbar spinal cord tissue was excised and fresh frozen with OCT in 2-methylbutane on dry ice. 10 μ m frozen sections were cut on the cryostat. Frozen sections were fixed in 4% PFA in PBS for 20 min and incubated in prechilled 70% ethanol for 30 min or longer at 4°C. Following rehydration in 40% formamide in 2 \times SSC for 10 min, the slides were blocked with hybridization solution (40% formamide, 2 \times SSC, 20 μ g/mL BSA, 100 mg/mL dextran sulfate, and 250 μ g/mL yeast tRNA, 2 mM Vanadyl Sulfate Ribonucleosides) for 30 min at 55 °C and then incubated with 200 ng/mL of denatured DNA probe (C2G4 \times 3-Cy-3 for sense foci and G4C2 \times 3-Cy-3 for antisense foci) in hybridization solution at 55 °C for 3 h. After hybridization the slides were washed three times with 40% formamide in 2 \times SSC and briefly washed one time in PBS. To co-stain with neuronal cells or motor neurons, the slides were then permeabilized in 0.5% triton X-100 in PBS for 15 min on ice and blocked in 2% normal goat or donkey serum in PBS for 1 hour. After blocking, the slides were incubated overnight at 4°C with NeuN (1:500, RRID: AB_177621, Millipore) or ChAT (1:200, RRID: AB_262156, Millipore) antibodies diluted in the blocking solution. The slides were then washed three times in PBS and incubated for 1 h at room temperature with goat anti-mouse conjugated to Alexa Fluor 488 (Invitrogen) or donkey anti-goat conjugated to Alexa Fluor 488 (Invitrogen) secondary antibodies at a dilution of 1:500. Slides were washed and autofluorescence of lipofuscin was quenched by 0.25% of Sudan Black B in 70% ethanol. Slides were mounted with mounting medium containing DAPI (Invitrogen) and imaged in 10 z-stacks (0.6 μ m between stacks) on a Leica confocal using a 63 \times water objective.

Immunohistochemistry. Animals were perfused transcardially with sterile 1x PBS and fresh tissue was harvested and stored in 10% formalin (Fisher Diagnostics) for 48 hours. Tissues were then moved into 70% ethanol. Tissue processing, embedding and sectioning were carried out by the histopathology core at the Center for Translational Research in Neurodegenerative Disease (CTRND), University of Florida. Five-micrometer sections were deparaffinized in xylene and rehydrated through graded ethanol. Antigen retrieval was performed by incubating the slides in a steamer with 10mM citrate buffer (pH 6.0) for 30 min or with 10mM EDTA (pH 6.4) for 12 min. The slides were washed for 10 min in running tap water and incubated in 95-100% formic acid for 5 min and subsequently washed for 10 min in running tap water. To prevent nonspecific binding and excessive background, slides were blocked with a serum free block or rodent block (Biocare Medical) for 15 min. Primary antibody was applied on the slides and incubated overnight at 4°C (see below for dilution information). Slides were washed with PBS and incubated with linking reagent (streptavidin or alkaline phosphatase; Covance) or biotinylated rabbit anti-goat IgG (Vector Labs) for 30 min at room temperature. After washing with 1XPBS, these sections were then incubated in 3% H₂O₂ (in methanol) for 15 min to block any endogenous peroxidase activity. Labeling reagent (HRP, Covance; Vectastain ABC-AP kit) was then applied to the slides for 30 min at room temperature. NovaRed and DAB (Vector Labs) was used to measure the peroxidase activity and the slides were counterstained with hematoxylin (modified Harris, Sigma Aldrich), rehydrated in graded alcohol and coverslipped for visualization. Images were taken on the Olympus BX51 microscope using the Cellsense software. For hematoxylin and eosin staining, the slides were deparaffinized in xylene and dehydrated through graded ethanol. The slides were then soaked in hematoxylin (modified Harris, Sigma Aldrich) for 1 min and washed in running distilled water for 10 min. Next, the slides were immersed in Eosin Y (Sigma Aldrich) for 30 sec and washed in distilled water for 10 min. The slides were rehydrated and coverslipped before visualization. For cresyl violet staining, slides were deparaffinized in xylene and subsequently dehydrated in graded ethanol. The slides were incubated in 0.25% cresyl violet at 60°C for 8-10 min and differentiated in 95% ethanol for 1-5 mins. Slides were then immersed in 100% ethanol and xylene and coverslipped for visualization.

Quantification. α -calbindin positive Purkinje neurons, thickness of the molecular layer, interneurons in the lumbar spinal cord, ChAT positive neurons, CV stained neurons and muscle fiber type were quantified using the cell counter plugin in ImageJ (National Institute of Health). Spinal cord sections per animal, 35 μ m apart were stained with α -ChAT or CV. The average numbers of ChAT positive or total neurons were quantified in each lumbar section. Only the neurons with a clear nucleolus were counted in each section. The quantitation was done in a blinded fashion by examining six lumbar sections (L2-L5), per slide, three slides per animal and 3 animals per group.

Antibodies used: In house mouse monoclonal α -poly-GA (1:1000 27B11 RRID: AB_2571626) and α -poly-GP (1:20,000 H3154 RRID: AB_2571627); α -choline acetyltransferase (1:150, RRID: AB_262156, Millipore); α -NeuN (1:500, RRID: AB_177621, Millipore); α -calbindin (1:250, RRID: AB_476894, Sigma-Aldrich); α -GFAP (1:5000, PU020-UP, BiogeneX); α -TARDBP (1:200, RRID: AB_615042, Proteintech); α -Iba-1 (1:500, RRID: AB_2224402, Abcam), α -My-32 (1:100, RRID: AB_477190, Sigma-Aldrich).

Antibody generation and validation. Mouse monoclonal α -poly-GA antibody (27B11) was generated to the repeat motif (GA₃₀) with New England Peptide. To validate the antibody with immunoblotting, recombinant poly-GA₃₀ was created using the Bac-to-Bac Baculovirus Expression System (Invitrogen). The recombinant protein were resolved in a 4-12% NuPAGE Bis-Tris gel (Invitrogen) and transferred onto a nitrocellulose membrane (Amersham). The membrane was blocked in 5% skim milk in PBS with 0.05% tween-20 (PBST) for 30 min. Primary antibody (α -poly-GA and α -Rb-flag) was added to the membrane and incubated overnight at 4°C. Anti-mouse and anti-rabbit-HRP-conjugated secondary antibodies were added to the membrane and incubated for an hour. ECL plus western blotting detection system (Amersham) was used to detect the bands. To validate the colocalization of poly-GA antibody and flag-epitope tag antibody, HEK293T cells were transfected with pcDNA 3.1 (GA)₃₀-flag and the empty plasmid pcDNA3.1. Transfected cells were rinsed with 1xPBS and fixed with 4% PFA in PBS for 30 min at room temperature followed by permeabilization with 0.5% Triton X-100 for 15 min on ice. The cells were washed with 1xPBS to remove any residual solution and 1% normal goat serum (NGS) was added to the cells as a blocking reagent. Antibodies were added and incubated for 1 h at room temperature. The slides were then washed again with 1xPBS and the secondary antibodies, goat anti-mouse conjugated to Cy3 (Jackson ImmunoResearch) and goat anti-rabbit conjugated to Alexa Fluor 488 (Invitrogen), was added at a dilution of 1:200. The slides were mounted with medium containing DAPI (Invitrogen).

Statistical analysis. Comparisons of RNA expression, statistical analysis of spinal roots, grip strength, open field, motor neuron count (α -ChAT), neuron count in brain and spinal cord (CV), muscle fiber type and Purkinje cell count were analyzed by unpaired t-test between the C9-BAC mice and non-transgenic littermates. Gait abnormalities were analyzed using the multiple t-test with the desired false discovery rate (FDR) set to 5%. Significant differences are indicated by “†”. Survival was analyzed by the Kaplan-Meier method, and the differences between groups were estimated by the Gehan-Breslow-Wilcoxon test. Population census analyses were analyzed by the chi-square test. All statistical analyses were performed using Prism 6.0 (GraphPad Software) with $p < 0.05$ considered statistically significant. The significance values in figures were indicated as follows: ns=not significant $p \geq 0.05$, * ($p < 0.05$); ** ($p \leq 0.01$); *** ($p \leq 0.001$); **** ($p \leq 0.0001$).

Supplemental Video Legends:

Video 1 (related to Figure 3). Example of an acute end-stage C9-BAC mouse with labored breathing and hind limb paralysis.

Video 2 (related to Figure 3). Example of an acute end-stage C9-BAC mouse with labored breathing and hindlimb and forelimb paralysis.

Video 3 (related to Figure 3). Slow progressive C9-BAC mouse showing reduced activity, kyphosis and hyperactivity when provoked compared to NT littermate.

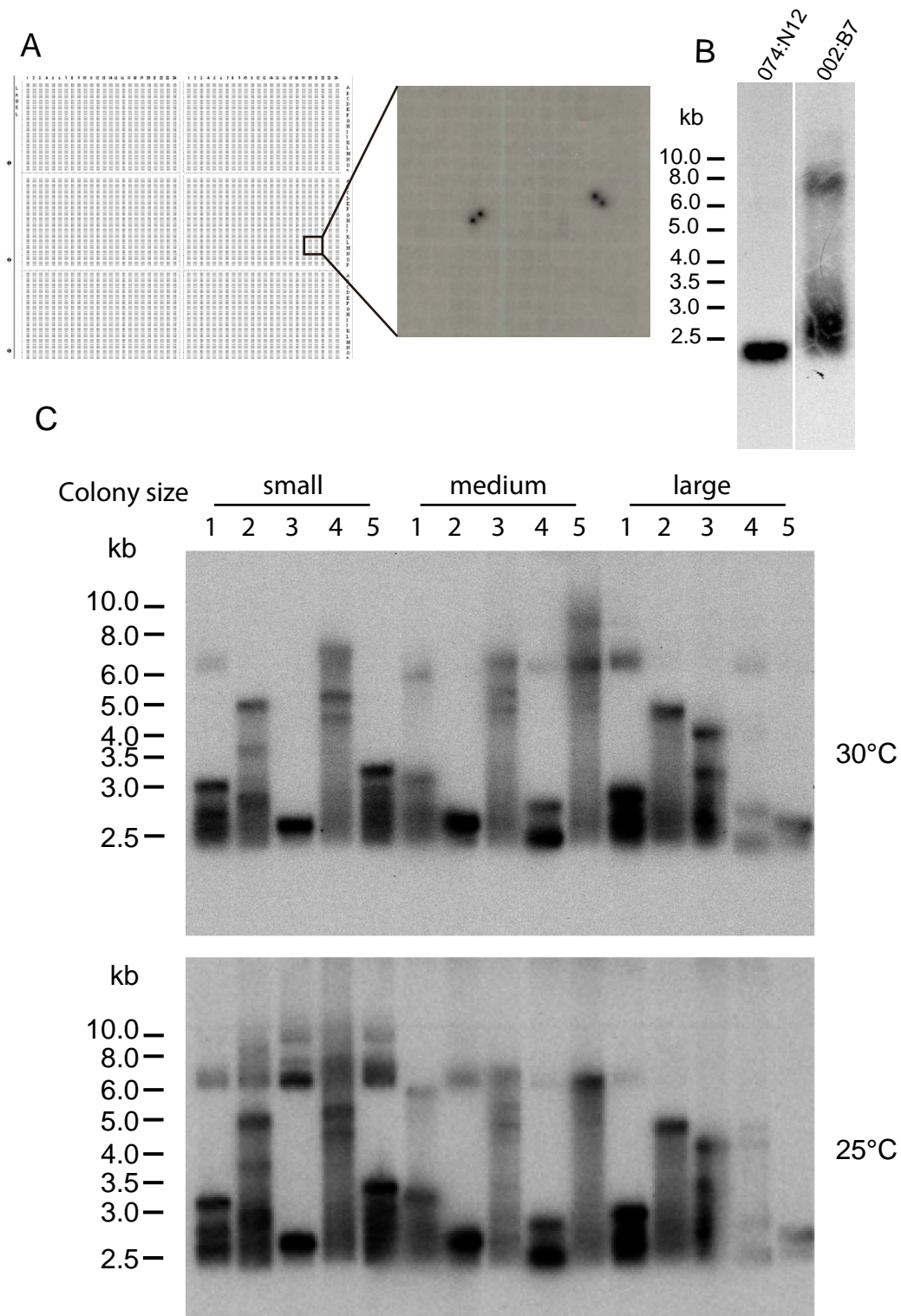


Figure S1 (related to Figure 1). BAC library screening and culturing of subclones to preserve G4C2 expansion.

(A) Schematic depiction of DNA filters (left panel) used to screen 39,936 clones with positive clones identified by hybridization to a radioactively labeled *C9orf72* probe (right panel).

(B) Southern blotting of *C9orf72* positive clones. 002:B7 contains the expanded allele and 074:N12 contains the normal allele.

(C) Southern blot analyses showing repeat instability in bacterial clones with different culture conditions. Single colonies from clone 002:B7 were selected based on colony size (small, medium and large) and sub-cultured at 30°C (top) or 25°C (bottom) on LB agarose plates.

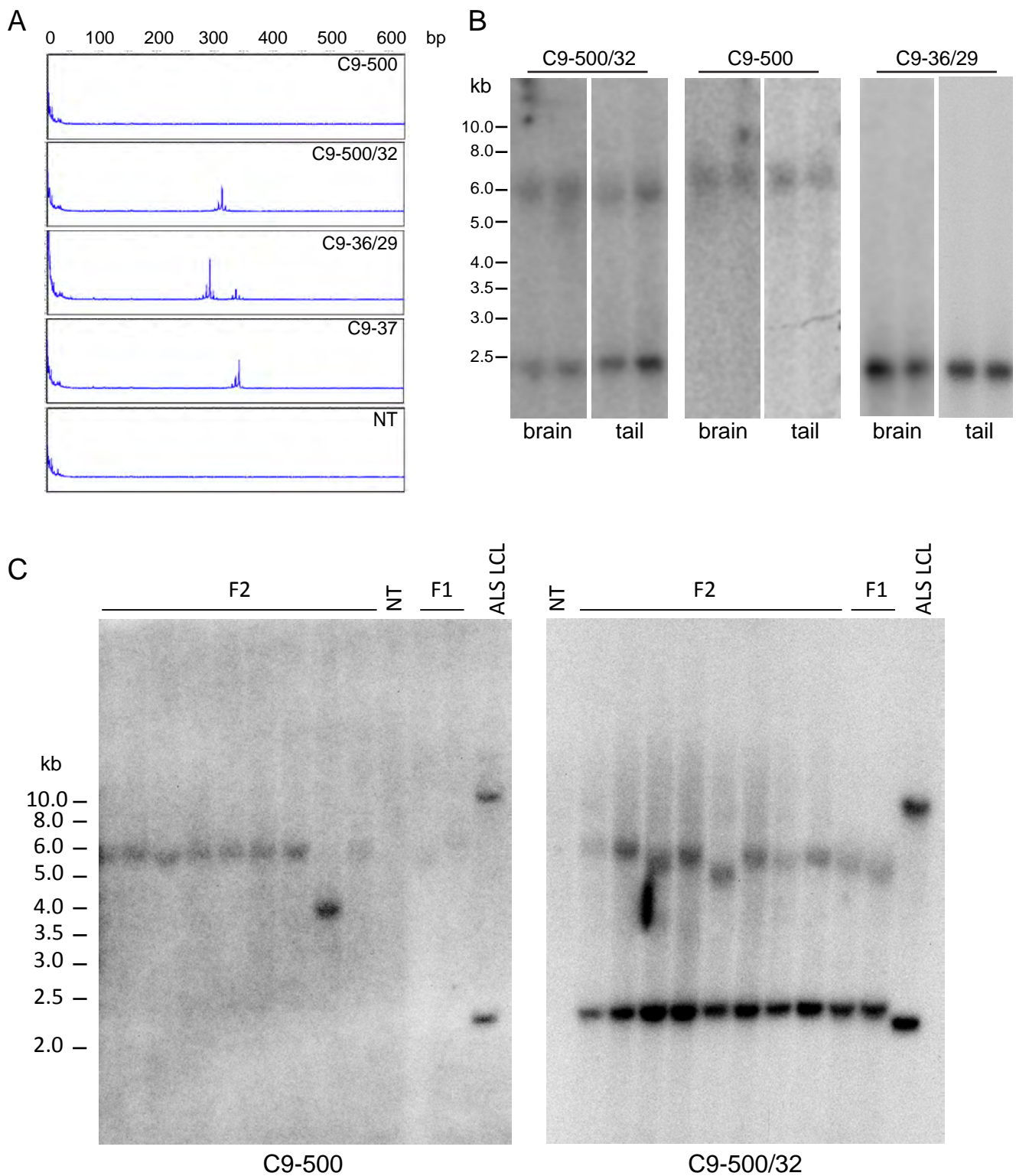


Figure S2 (related to Figure 1). Repeat size and instability in C9-BAC mice.

(A) Fluorescent labeled fragment analyses to determine the length of the shorter alleles in the various C9-BAC lines and a NT control.

(B) Southern analysis showing similar repeat sizes in brain and tail DNA samples in C9-500/32, C9-500 and C9-36/29 lines (two representative animals per line).

(C) Southern blotting showing ~500 G4C2 repeats were maintained in most of the animals when the transgene was transmitted from the F1 to the F2 generation in both the C9-500/32 and C9-500 lines.

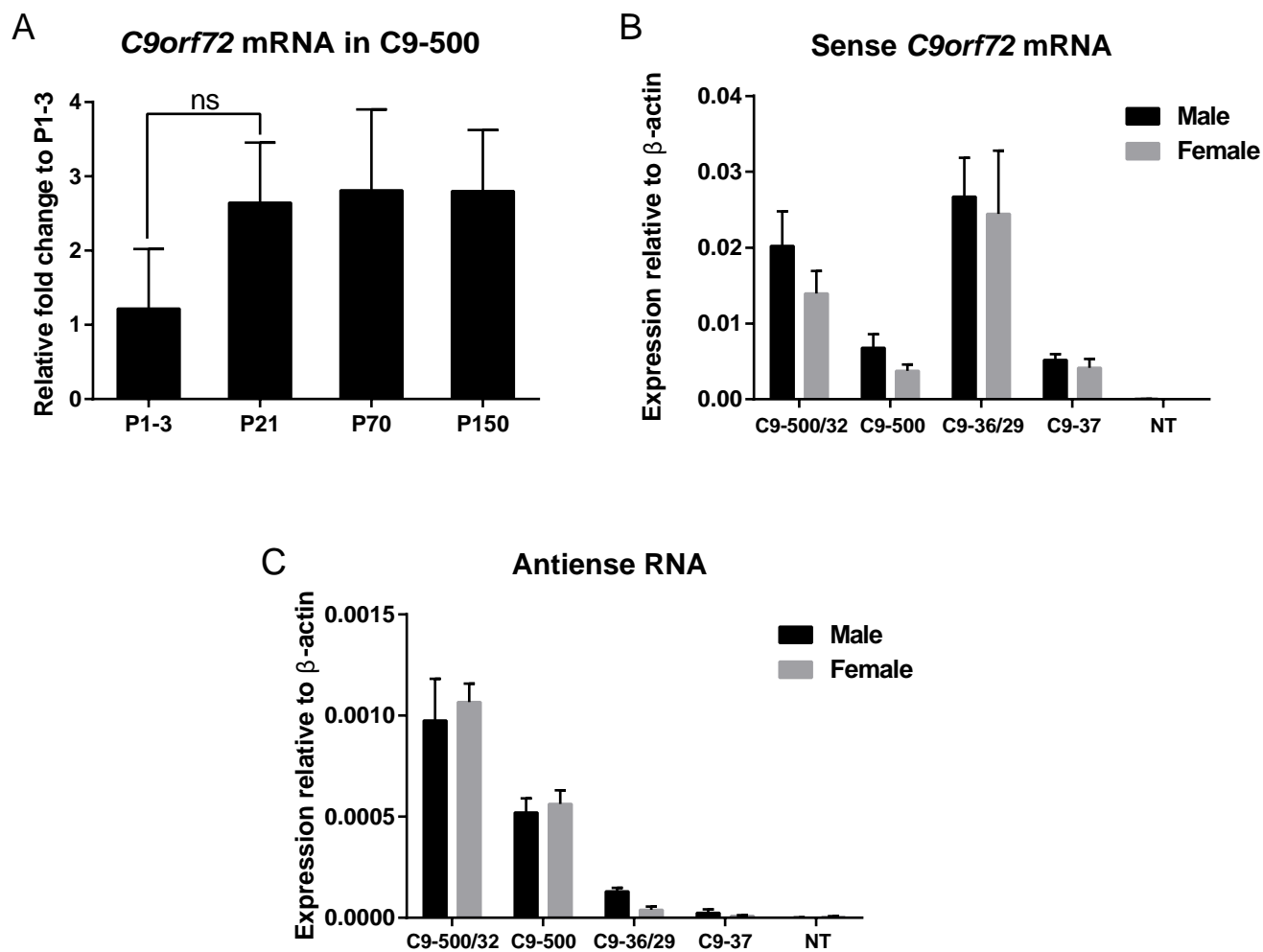


Figure S3 (related to Figure 2). Time course of *C9orf72* expression and comparable *C9orf72* and antisense RNA levels in frontal cortex in males and females at 2 months of age.

(A) Time course of the expression of *C9orf72* in the frontal cortex from the C9-500 line. n=3 per time point, mean + SD, unpaired t test, ns p >0.05 vs. NT shown.

(B) qRT-PCR of *C9orf72* all variants. Male n=4, female n=3.

(C) qRT-PCR of antisense RNAs. Male n=4, female n=3.

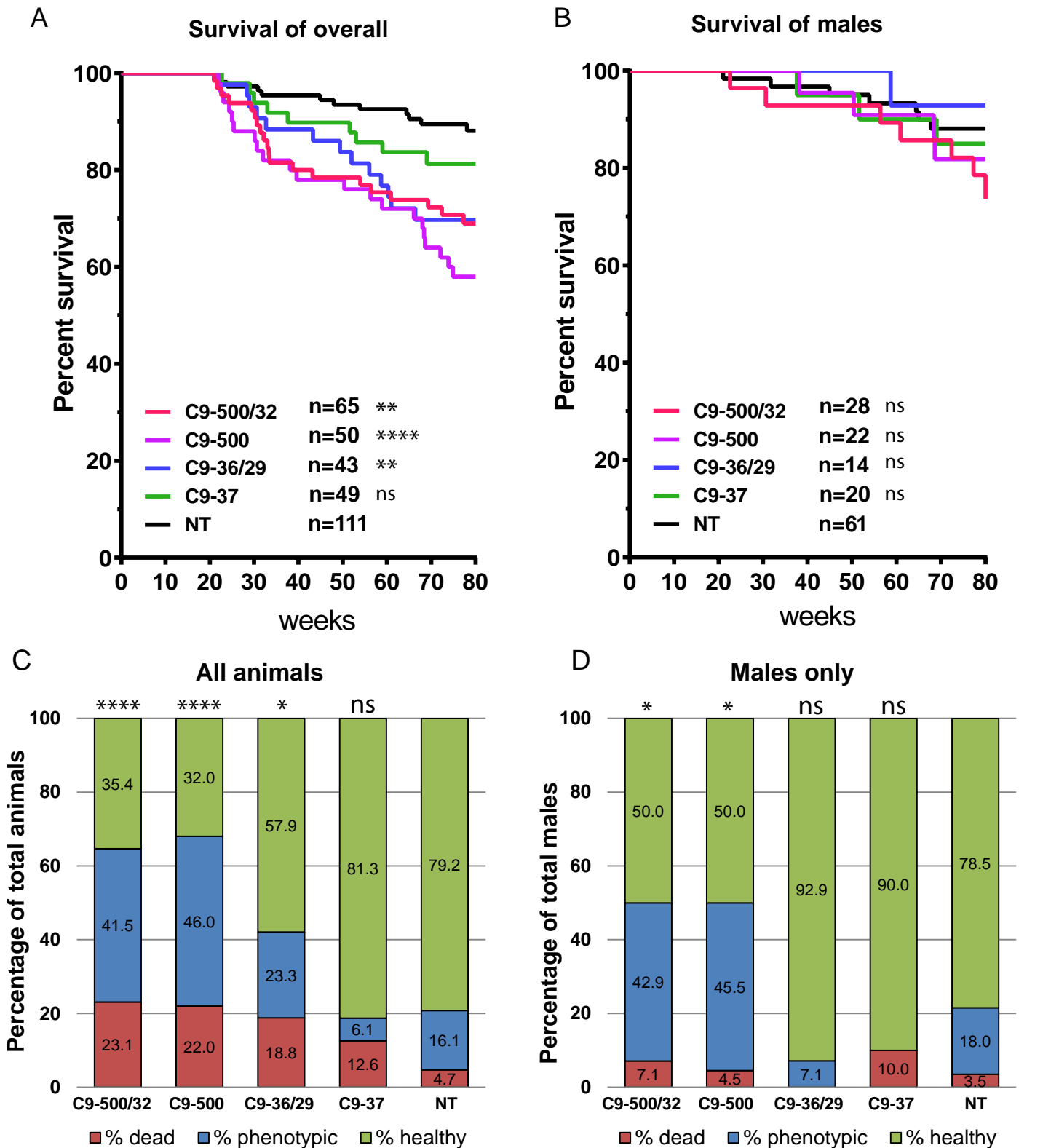


Figure S4 (related to Figure 3). Survival curves and population analyses of all animals and male animals.

(A) Kaplan-Meier curve of male and female C9-BAC expansion mice show decreased survival in the C9-500/32, C9-500, C9-36/29 compared to NT littermates. NT littermate n=111, C9-500/32 n=65, C9-500 n=50, C9-36/29 n=43, C9-37 n=49, mean + SD, Gehan-Breslow-Wilcoxon test, ** p<0.01, **** p<0.0001, ns p>0.05 vs. NT.

(B) Kaplan-Meier curve of male C9-BAC mice show no significant decrease in survival across multiple lines. NT littermate n=61, C9-500/32 n=28, C9-500 n=22, C9-36/29 n=14, C9-37 n=20, mean + SD, Gehan-Breslow-Wilcoxon test, ns p>0.05 vs. NT.

(C) Population census plot of male and female animals showing percentage of dead (red), phenotypic (blue) and healthy (green) animals at one year of age. NT littermate n=111, C9-500/32 n=65, C9-500 n=50, C9-36/29 n=43, C9-37 n=49, mean + SD, Chi square test, ****p<0.0001, * p<0.05, ns p>0.05 vs. NT.

(D) Population census plot of male animals at one year of age. NT littermate n=61, C9-500/32 n=28, C9-500 n=22, C9-36/29 n=14, C9-37 n=20, mean + SD, Chi square test, * p<0.05, ns p>0.05 vs. NT.

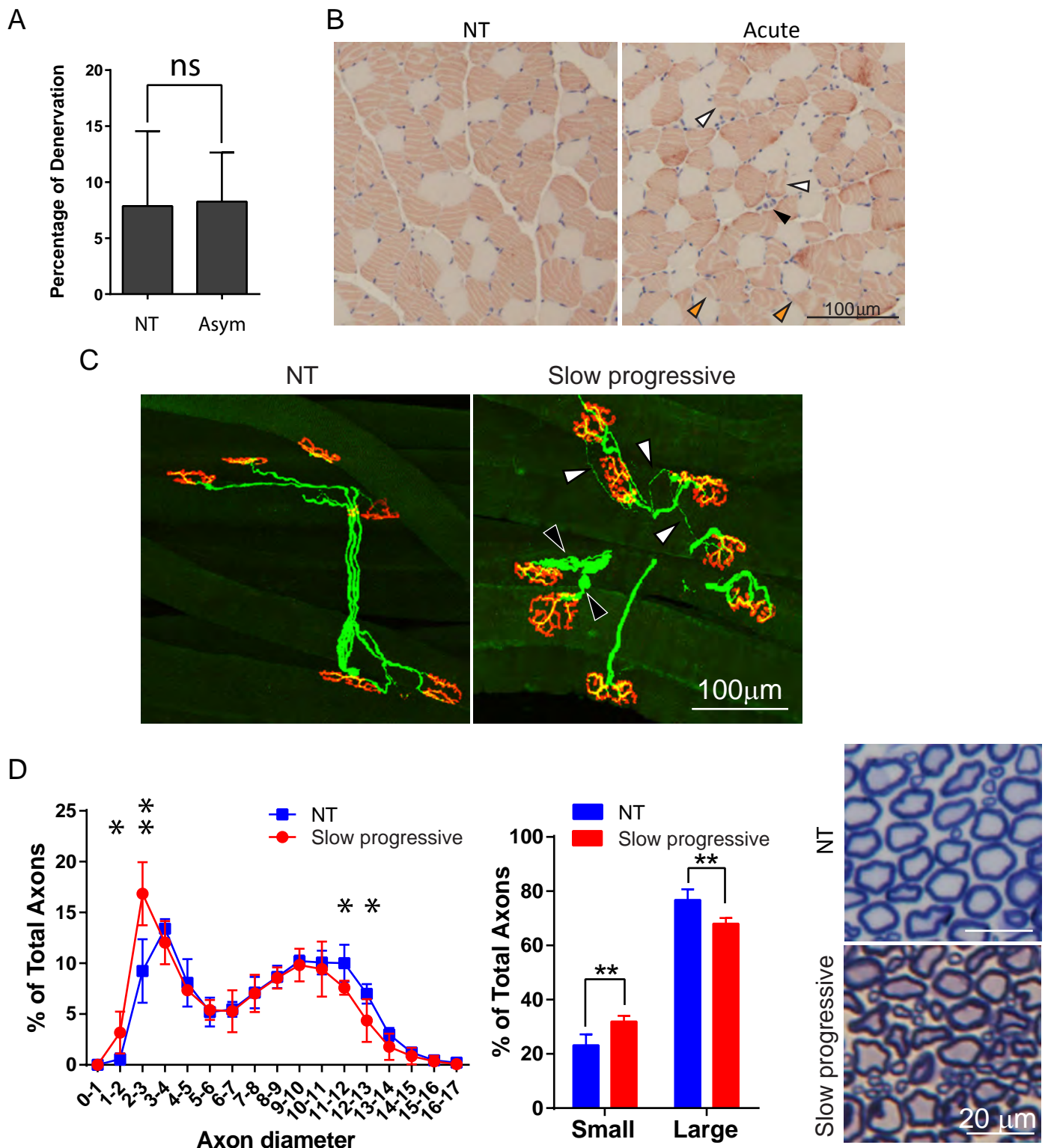


Figure S5 (Related to Figure 4). Neuromuscular junction and muscle abnormalities in C9-BAC mice.

(A) Quantification of NMJ in tibialis anterior muscle showed no significant differences between NT and asymptomatic animals. NT n=3, Asym n=3, mean ± SD, unpaired t test, ns p>0.05 vs NT.

(B) Muscle immunohistochemistry using anti-Myosin-32 antibody shows atrophic fibers (white arrow), pyknotic nuclear clumps (black) and sharp angular fibers (orange) in the acute mice but not in NT animals.

(C) Axonal terminal swelling (black arrows) and sprouting (white arrows) of tibialis anterior muscle in slow progressive C9-BAC mouse. Neuromuscular junctions (red, acetylcholine receptors labeled with α -bungarotoxin tetramethylrhodamine conjugate), motor axons and synapses (green, labeled with anti-neurofilament H antibody).

(D) Left panel, axon size distribution of spinal cord lumbar 4 ventral roots from C9-BAC slow progressive animals (~18-month-old, red) and age matched NT littermates (blue) animals. Middle panel, slow progressive animals (red) show increased number of axons with smaller diameter and decreased axons with larger diameter compared to age matched NT littermates (blue). Right panel, representative image of spinal cord lumbar 4 ventral roots with toluidine blue staining from a slow progressive animal. NT n=5, slow progressive n=4, mean + SD unpaired t test, **p<0.01, *p<0.05 vs. NT.

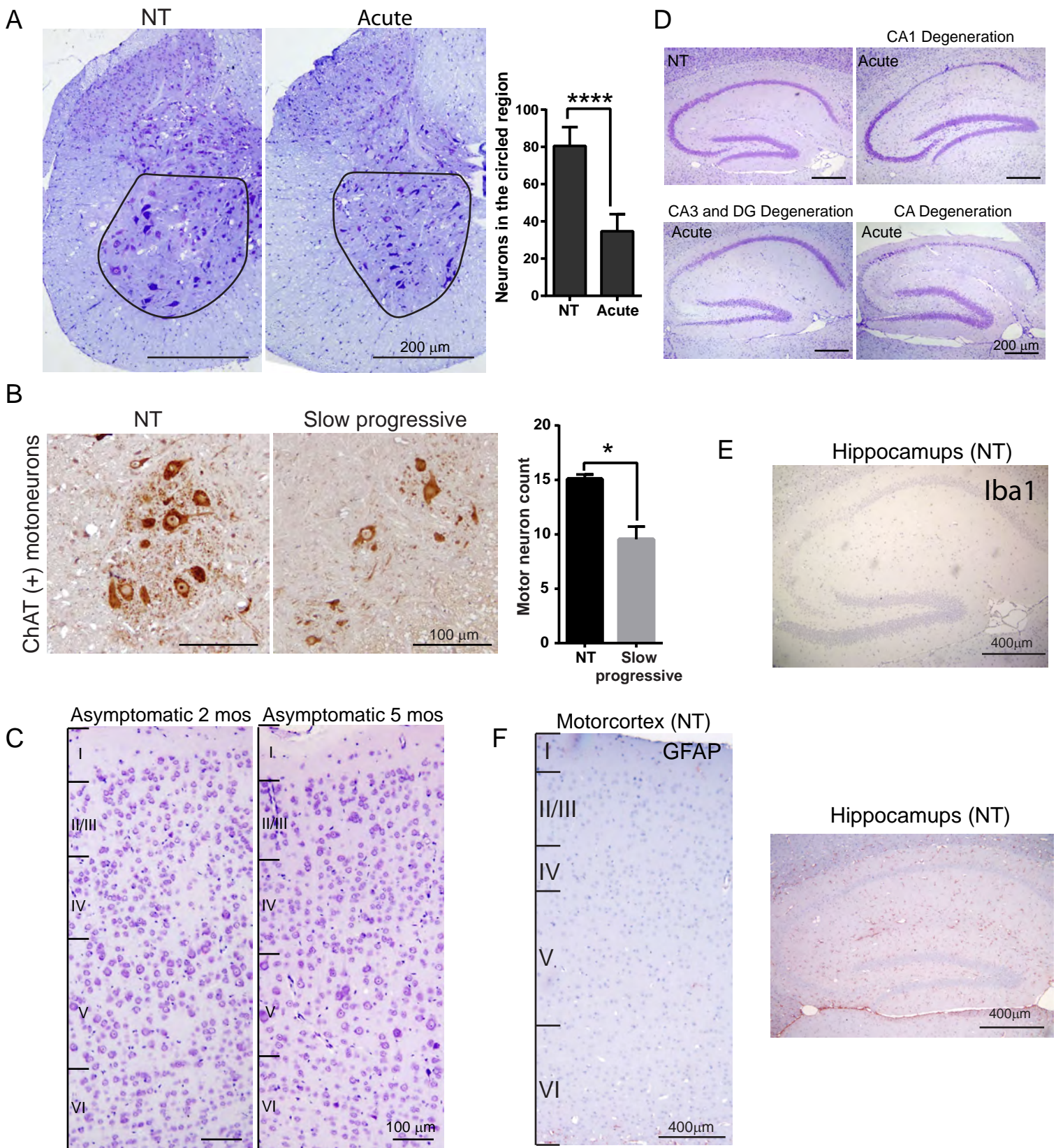


Figure S6 (Related to Figures 4-6 and Table 1). Additional characterization of neurodegeneration in the spinal cord and cortex of the C9-BAC mice.

(A) Cresyl violet staining of the lumbar spinal cord (right panel) and quantification (left panel) shows a significant loss of all neurons in the circled region, mean \pm SEM, NT n=3, acute n=3, unpaired t test, ****p<0.0001 vs NT.

(B) Left panel, IHC staining using anti-ChAT antibody. Right panel, quantification of ChAT positive motor neurons from lumbar spinal cord. NT n=3, acute n=3, mean \pm SEM, unpaired t test, *p<0.05 vs. NT.

(C) No overt neurodegeneration is seen in layer II/III or layer V of the motor cortex in the asymptomatic 2 month or 5 month old C9-BAC mice.

(D) Cresyl violet staining of the hippocampus shows pyknotic neurons in the CA1 region, CA3 and dentate gyrus and the entire CA region of acute end-stage animals but not in NT controls.

(E) IHC staining of the hippocampus of age matched NT littermate control with anti-Iba 1 antibody.

(F) IHC staining of the cortex and hippocampus of age matched NT littermate controls with anti-GFAP antibody.

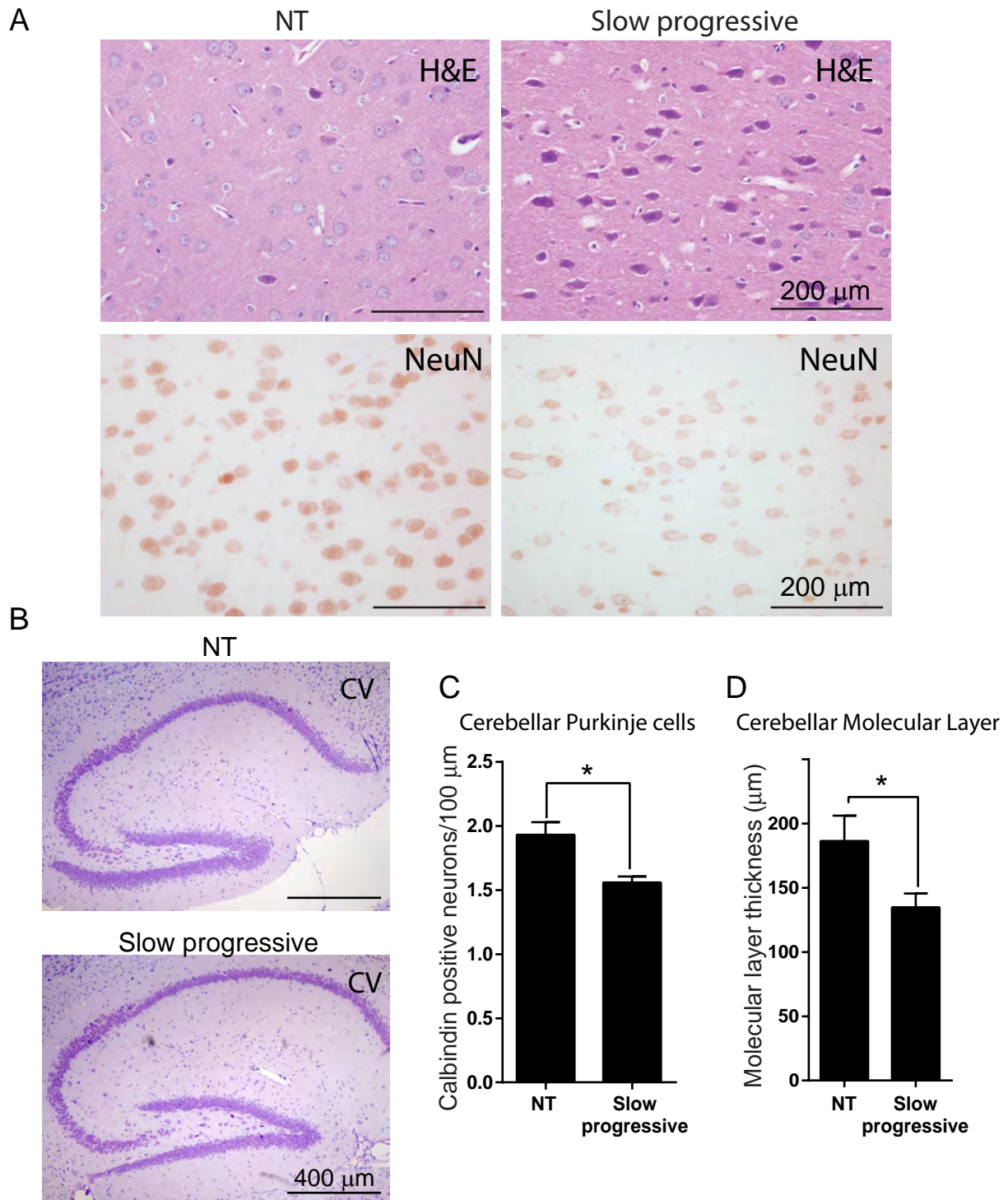


Figure S7 (Related to Figures 5 and 6 and Table 1). Neurodegeneration in motor cortex and cerebellum of slow progressive C9-BAC animals.

(A) H&E (upper panel) and IHC with anti-Neu-N antibody (lower panel) of motor cortex of NT and C9-BAC aged phenotypic animals.

(B) Cresyl violet staining of the hippocampus shows no neurodegeneration in the slow progressive mice compared to the NT controls.

(C) Quantification of cerebellar anti-calbindin antibody positive Purkinje cells. NT n=3, slow progressive n=3, mean + SEM, unpaired t test, *p<0.05 vs. NT.

(D) Quantification of cerebellar molecular layer thickness. NT n=3, slow progressive n=3, mean + SEM, unpaired t test, *p<0.05 vs. NT.

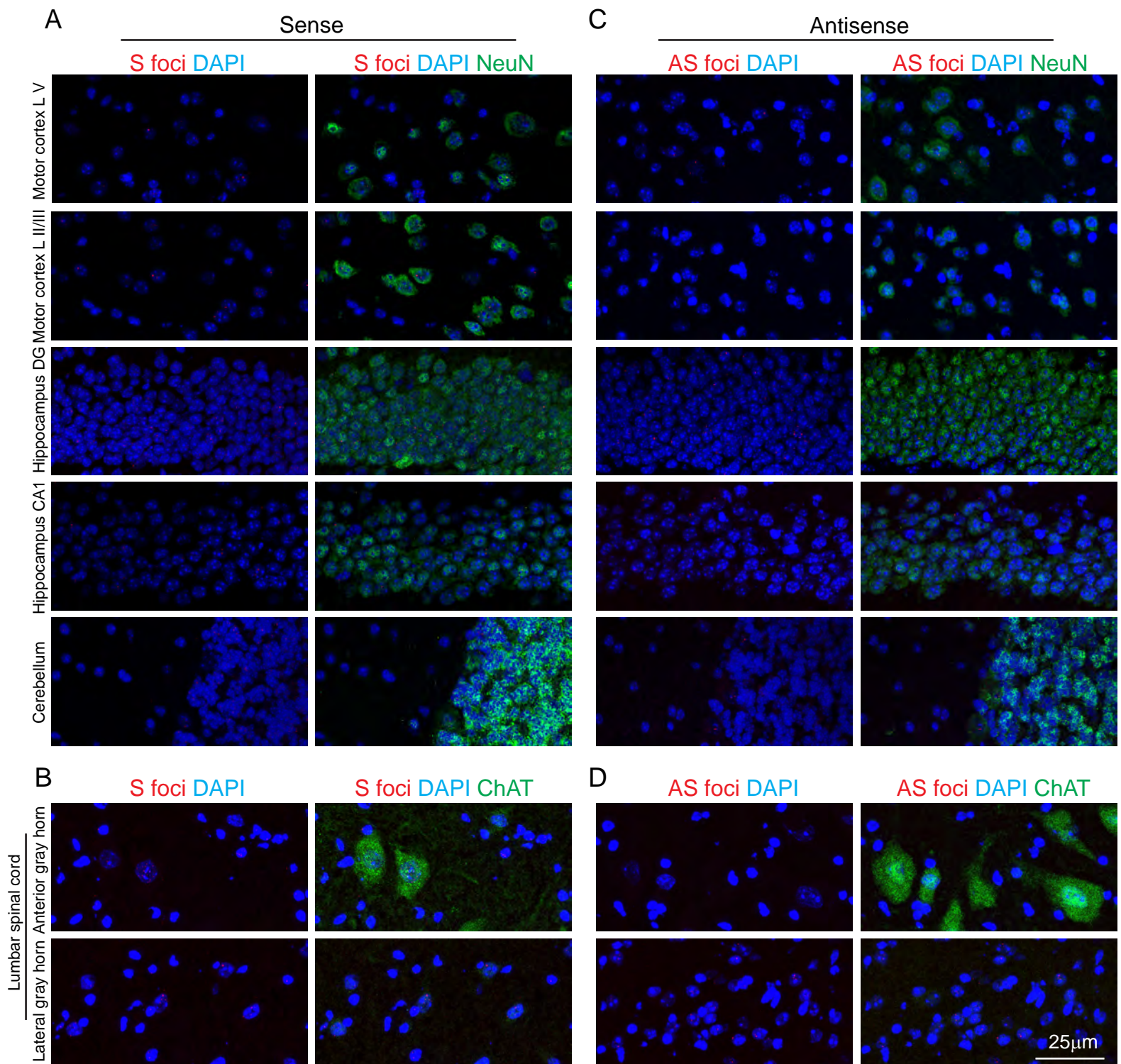


Figure S8 (Related to Figure 7 and Table 1). Two-month old C9-BAC expansion mice show sense and antisense RNA foci in multiple regions of CNS.

(A) FISH-IF co-staining sense foci with anti-Neu-N antibody to mark neuronal cells in C9-500 mouse brain. Left panel, sense foci (red) with DAPI nuclear staining (blue). Right panel, merged image with sense foci (red), DAPI nuclear staining (blue) and NeuN staining (green).

(B) FISH-IF co-staining sense foci with lower motor neurons in C9-500 mouse spinal cord. Left panel, sense foci (red) with DAPI nuclear staining (blue). Right panel, merged image with sense foci (red), DAPI nuclear staining (blue) and anti-ChAT staining (green).

(C) FISH-IF co-staining antisense foci with neuronal cells in C9-500 mouse brain. Left panel, antisense foci (red) with DAPI nuclear staining (blue). Right panel, merged image with antisense foci (red), DAPI nuclear staining (blue) and anti-NeuN staining (green).

(D) FISH-IF co-staining antisense foci with lower motor neurons in C9-500 mouse spinal cord. Left panel, antisense foci (red) with DAPI nuclear staining (blue). Right panel, merged image with antisense foci (red), DAPI nuclear staining (blue) and anti-ChAT staining (green).

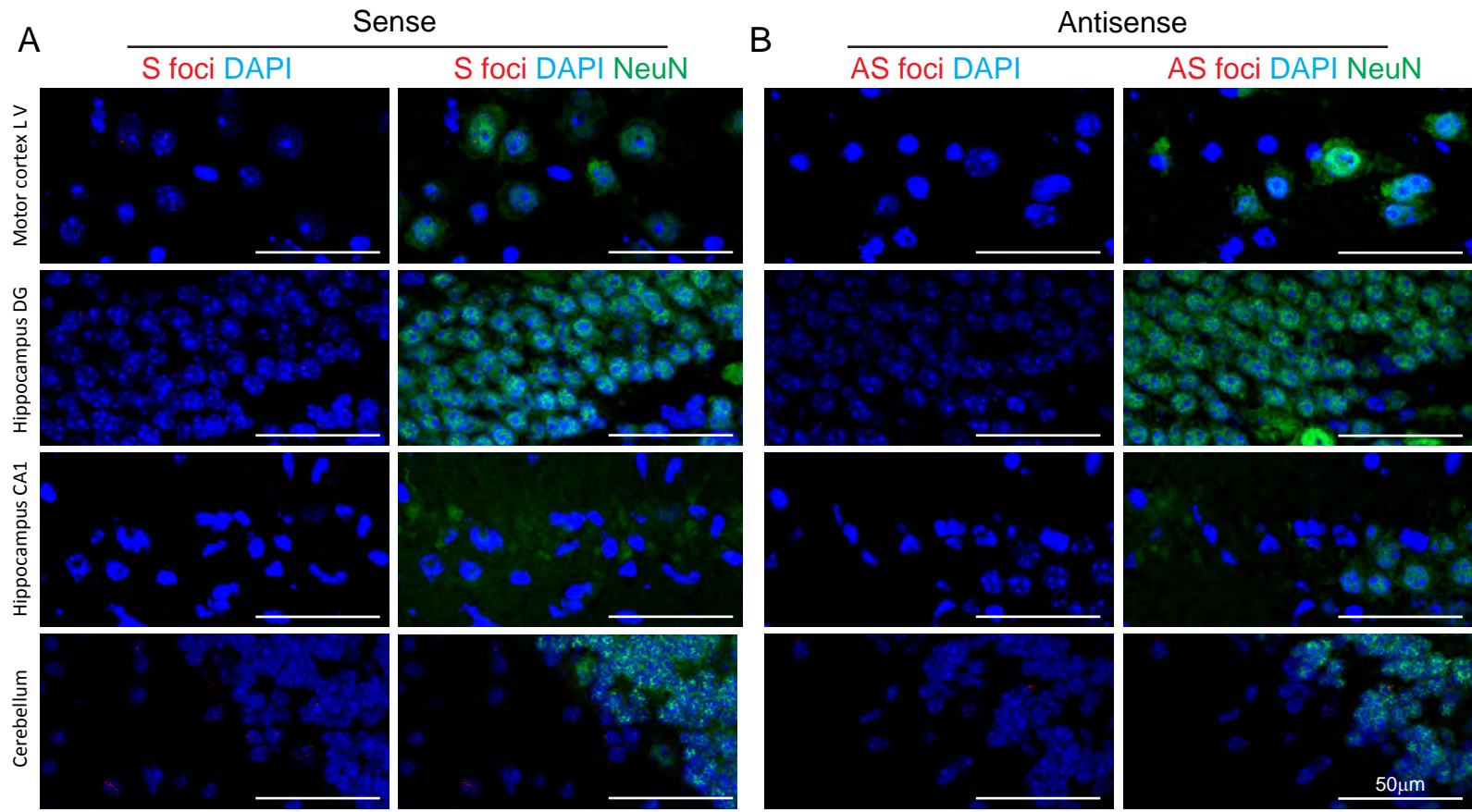


Figure S9 (Related to Figure 7 and Table 1). C9-BAC acute end-stage mice show sense and antisense RNA foci in remaining cells of the brain.

(A) FISH-IF co-staining of sense foci with cells in C9-500 acute end-stage mouse brain. Right panel, sense foci (red) with DAPI nuclear staining (blue). Left panel, merged image with sense foci (red), DAPI nuclear staining (blue) and anti-NeuN staining (green).

(B) FISH-IF costaining antisense foci with neuronal cells in C9-500 acute end-stage mouse brain. Right panel, antisense foci (red) with DAPI nuclear staining (blue). Left panel, merged image with antisense foci (red), DAPI nuclear staining (blue) and anti-NeuN staining (green).

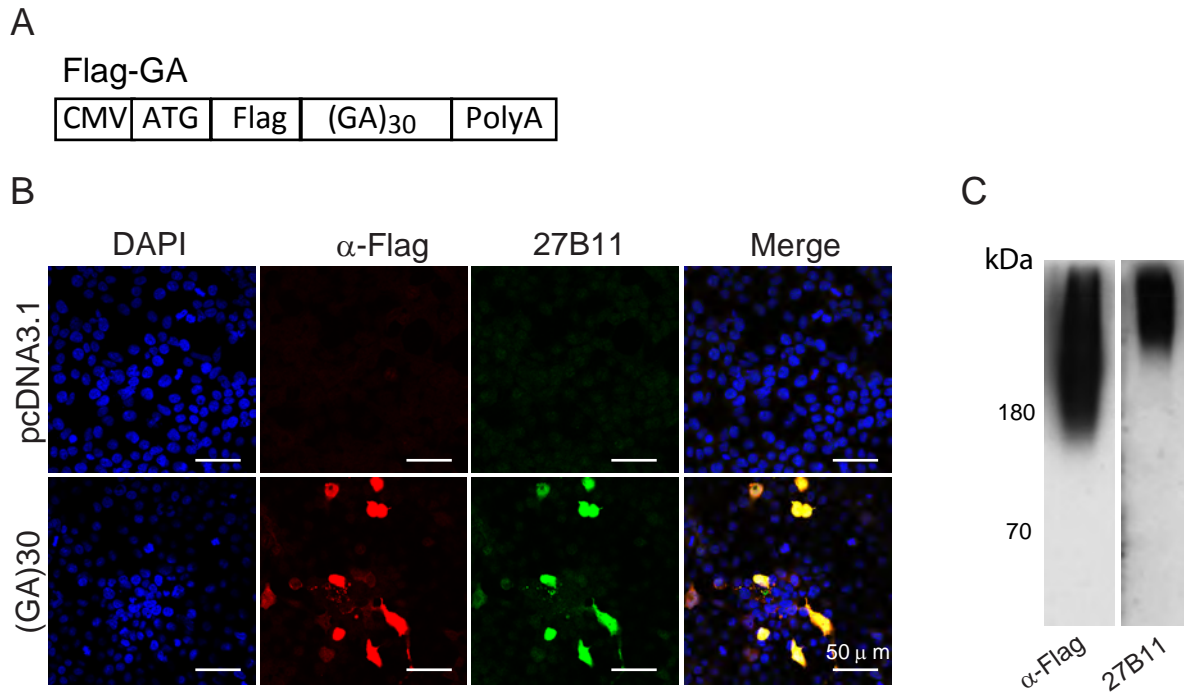


Figure S10 (Related to Figure 7). Validation of monoclonal poly-GA antibody (27B11).

(A) Schematic diagram of flag epitope tag construct used for validation of anti-poly-GA antibody (27B11).

(B) IF co-staining flag-tag (anti-flag antibody, green) and poly-GA protein (anti-poly-GA 27B11, red) in HEK293T cells transfected with flag-(GA)₃₀ construct or pcDNA 3.1 vector control.

(C) Immunoblots of flag-(GA)₃₀ recombinant protein with anti-flag and anti-poly-GA (27B11) antibodies.

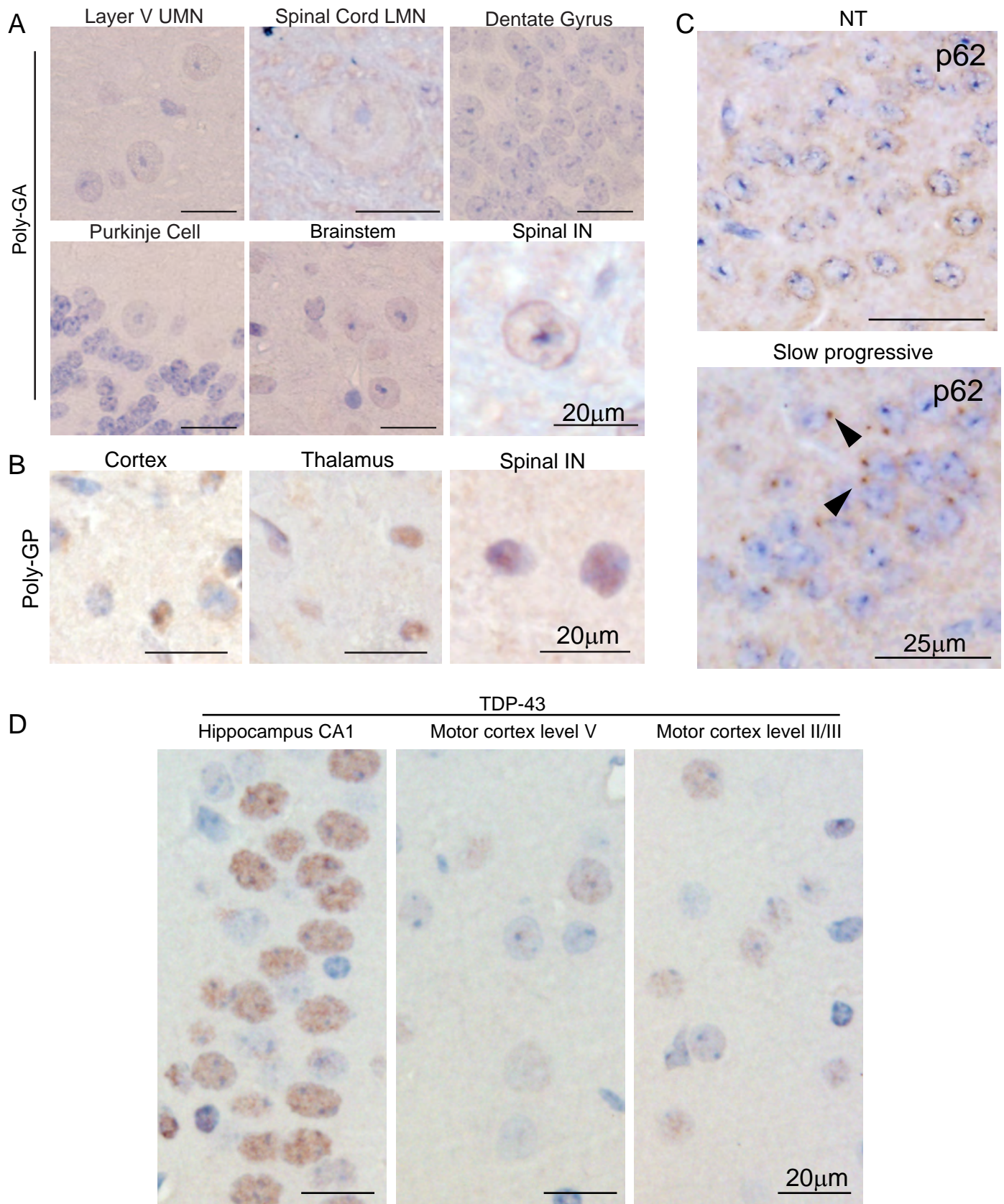


Figure S11 (Related to Figure 7). P62 in C9-BAC mice and IHC staining of NT littermates to C9-BAC mice.

(A) IHC staining of age matched NT littermate controls with anti-poly-GA (27B11A7) antibody.

(B) IHC staining of age matched NT littermate controls with anti-poly-GP (H3154) antibody.

(C) p62 staining of the retrosplenial cortex shows abundant perinuclear staining in the slow progressive mice but not the NT controls.

(D) IHC staining of age matched NT littermate controls with anti-TDP-43 antibody.

Table S1 (Related to Figure 1 and 2). Primers used for PCR

Primer Name	Primer Sequence (5' to 3')
ASORF-F	AGTCGCTAGAGGCGAAAGC
ASORF-R	CGAGTGGGTGAGTGAGGAG
C9mRNA-F	TCTCCAGCTGTTGCCAAGAC
C9mRNA-R	TCCATTCTCTCTGTGCCTTCT
1a-F	GCCCACGTAAAAGATGACGC
1a-R	CCTCCTAAACCCACACCTGC
mACT-F	TCGTGCGTGACATCAAAGAG
mACT-R	GATCTTCATGGTGCTAGGAG
mC9-F	CCTGATGTCAGGTGCATCGT
mC9-R	GAGGGGCAGGAAGTCAACTC
Probe-F	AGAACAGGACAAGTTGCC
Probe-R	AACACACACCTCCTAAACC
C9GT-F	AGTTGGGTCCATGCTCAACAA
C9GT-R	ACTGTTCTAGGTACCGGGCT
pCC1-F	GGATGTGCTGCAAGGCGATTAAGTTGG
pCC1-R	CTCGTATGTTGTGTGGAATTGTGAGC

Table S2 (Related to Figure 3). Digitgait analysis of four to five month old mice (combination of male and female)

Parameters (42 in total)	Unit	C9500/32 Vs. NT	C9-500 Vs. NT	C9-36/29 Vs. NT
Significant Parameters (Desired FDR=5%)	(real#)	14	4	0
Swing	(s)	↑† p=0.0065	↑† p=0.0036	ns
Swing/Stride	(%)	↑† p=0.0015	↑† p=0.0007	ns
Brake	(s)	ns	ns	ns
Brake/Stride	(%)	ns	ns	ns
Propel	(s)	ns	ns	ns
Propel/Stride	(%)	↓† p=0.008	ns	ns
Stance	(s)	ns	ns	ns
Stance/Stride	(%)	↓† p=0.0015	↓† p=0.0007	ns
Stride	(s)	ns	ns	ns
Brake/Stance	(%)	ns	ns	ns
Propel/Stance	(%)	ns	ns	ns
Stance/Swing	(real#)	↓† p=0.0025	↓† p=0.0016	ns
Stride Length	(cm)	ns	ns	ns
Stride Frequency	(steps/s)	ns	ns	ns
Paw Angle	(deg)	ns	ns	ns
Absolute Paw Angle	(deg)	ns	ns	ns
Paw Angle Variability	(deg)	ns	ns	ns
Stance Width	(cm)	ns	ns	ns
Step Angle	(deg)	ns	ns	ns
Stride Length Variability	(cm)	↓† p=0.0019	ns	ns
SWVar Variability	(cm)	ns	ns	ns
Stance Width Variability	(deg)	ns	ns	ns
#Steps	(real#)	ns	ns	ns
Stride Length CV	(CV%)	↓† p=0.0015	ns	ns
Stance Width CV	(CV%)	ns	ns	ns
Step Angle CV	(CV%)	ns	ns	ns
Swing Duration CV	(CV%)	ns	ns	ns
Paw Area at Peak Stance	(cm ²)	↓† p=0.0011	ns	ns
Paw Area Variability at Peak Stance	(cm ²)	↓† p=0.0016	ns	ns
Hind Limb Shared Stance Time	(s)	ns	ns	ns
Shared/Stance	(%)	ns	ns	ns
Stance Factor	(real#)	ns	ns	ns
Gait Symmetry	(real#)	ns	ns	ns
MAX dA/dT	(cm ² /s)	↓† p=0.0004	ns	ns
MIN dA/dT	(cm ² /s)	↑† p=0.0097	ns	ns
Tau - Propulsion	(real#)	↓† p=0.0018	ns	ns
Overlap Distance	(cm)	ns	ns	ns
Paw Placement Positioning	(cm)	ns	ns	ns
Ataxia Coefficient	(real#)	ns	ns	ns
Midline Distance	(cm)	↑† p=0.0015	ns	ns
Axis Distance	(cm)	ns	ns	ns
Paw Drag	(mm ²)	↓† p=0.0008	ns	ns

#, number; ↑, upregulated; ↓, downregulated; CV, coefficient of variation; ns, not significant in Multiple t tests; †, significant in Multiple t tests, desired FDR (false discovery rate) set to 5%; C9-500 n=14; C9-500/32 n=16; C9-36/29 n=11; NT n=21.